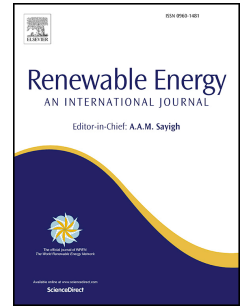


# Journal Pre-proof

The development, design and characterisation of a scale model Horizontal Axis Tidal Turbine for dynamic load quantification

Matthew Allmark, Robert Ellis, Catherine Lloyd, Stephanie Ordonez-Sanchez, Kate Johannesen, Carl Byrne, Cameron Johnstone, Tim O'Doherty, Allan Mason-Jones



PII: S0960-1481(20)30592-9

DOI: <https://doi.org/10.1016/j.renene.2020.04.060>

Reference: RENE 13389

To appear in: *Renewable Energy*

Received Date: 12 June 2019

Revised Date: 25 March 2020

Accepted Date: 10 April 2020

Please cite this article as: Allmark M, Ellis R, Lloyd C, Ordonez-Sanchez S, Johannesen K, Byrne C, Johnstone C, O'Doherty T, Mason-Jones A, The development, design and characterisation of a scale model Horizontal Axis Tidal Turbine for dynamic load quantification, *Renewable Energy* (2020), doi: <https://doi.org/10.1016/j.renene.2020.04.060>.

This is a PDF file of an article that has undergone enhancements after acceptance, such as the addition of a cover page and metadata, and formatting for readability, but it is not yet the definitive version of record. This version will undergo additional copyediting, typesetting and review before it is published in its final form, but we are providing this version to give early visibility of the article. Please note that, during the production process, errors may be discovered which could affect the content, and all legal disclaimers that apply to the journal pertain.

© 2020 Published by Elsevier Ltd.

## Author Credit Statement:

Methodology	Matthew Allmark, Stephanie Ordonez, Kate Johannesen
Software	Matthew Allmark, Stephanie Ordonez, Rob Ellis
Validation	Matthew Allmark, Stephani Ordonez
Formal analysis	Matthew Allmark
Investigation	Matthew Allmark, Rob Ellis, Stephanie Ordonez, Catrherine Lloyd, Allan Mason-Jones
Resources	Matthew Allmark, Carl Byrne, Tim O'Doherty
Data Curation	Matthew Allmark
Writing - Original Draft	Matthew Allmark
Writing - Review & Editing	Matthew Allmark, Tim O'Doherty, Stephanie Ordonez
Visualization	Matthew Allmark
Supervision	Tim O'Doherty, Cameron Johnstone
Project administration	Tim O'Doherty, Cameron Johnstone
Funding acquisition	Tim O'Doherty, Cameron Johnstone, Matthew Allmark

# The development, design and characterisation of a scale model Horizontal Axis Tidal Turbine for Dynamic Load Quantification.

Matthew Allmark<sup>a,\*</sup>, Robert Ellis<sup>a</sup>, Catherine Lloyd<sup>a</sup>, Stephanie Ordonez-Sanchez<sup>b</sup>, Kate Johannesen<sup>b</sup>, Carl Byrne<sup>a</sup>, Cameron Johnstone<sup>b</sup>, Tim O'Doherty<sup>a</sup>, Allan Mason-Jones<sup>a</sup>

<sup>a</sup>Cardiff University School of Engineering, Cardiff, CF24 3AA United Kingdom

<sup>b</sup>Department of Mechanical and Aerospace Engineering University of Strathclyde, James Weir Building, Level 8, 75 Montrose Street, Glasgow, G1 1XJ

---

## Abstract

The paper describes the development and characterisation of three 0.9 m diameter lab-scale Horizontal Axis Tidal Turbines. The blade development process has been outlined and was used to generate a design specification. Each turbine houses instrumentation to measure rotor thrust, torque and blade root bending moments on each blade, in both 'flapwise' and 'edgewise' directions. A permanent magnet synchronous machine and encoder are integrated to allow for servo-control of the turbine as well as to provide position and rotational velocity measurements, resulting in three turbines that can be individually controlled using speed or torque control. **Analogue signals**

---

\*Corresponding author

*Email addresses:* AllmarkMJ1@cardiff.ac.uk (Matthew Allmark), EllisR10@cardiff.ac.uk (Robert Ellis), LloydC11@cf.ac.uk (Catherine Lloyd), s.ordonez@strath.ac.uk (Stephanie Ordonez-Sanchez), kate.porter.10@alumni.ucl.ac.uk (Kate Johannesen), byrne@cardiff.ac.uk (Carl Byrne), cameron.johnstone@strath.ac.uk (Cameron Johnstone), Odoherty@cardiff.ac.uk (Tim O'Doherty), mason-jonesA@cardiff.ac.uk (Allan Mason-Jones)

are captured via a real-time operating system and field programmable gate array hardware architecture facilitating sample rates of up to 2 kHz. Results from testing the pilot turbine at three differing facilities during the development process are presented. Here good agreement, less than 7% variation, was found when comparing the testing undertaken at various flume and tow tank facilities. Lastly, the findings of a test campaign to characterise the performance of each of the three turbines are presented. Very good agreement in non-dimensional values for each of the three manufactured turbines was found.

*Keywords:* Horizontal Axis Tidal Turbine, Scale Turbine Development, Computational Fluid Dynamics, ANSYS CFX, Turbine Characterisation

---

## 1. Introduction

Energy extraction from the ocean's tides has gained widespread acceptance as a potential contributor to the UK energy mix [1]. Increased interest in tidal energy extraction has, in part, been driven by the realisation of finite global resources and environmental impacts of burning fossil fuels [2]. The EU Renewable Energy Directive has recently extended previous commitments to stipulate that the EU community will fulfil 35% of its energy needs via updated citataion renewable sources by 2030; it is foreseen that tidal energy extraction could go some way to helping achieve this target [3].

In order for Horizontal Axis Tidal Turbine (HATT) devices to generate energy at a competitive levelized cost of energy (LCOE), effective strategies for reducing device over-engineering and the burden of operation and maintenance costs are required. In order to achieve the 20 year lifespan [4] -

14 quoted as being required for cost effective energy extraction - whilst reducing  
15 device over engineering, detailed understanding of HATT operational loads  
16 is required. Knowledge of normal operational loads, extreme operational  
17 loads and the characteristics of load fluctuations is required to minimise the  
18 probability of device failure due to overloading and fatigue.

19 During the projected turbine life cycle, extreme loads can arise from  
20 current-wave interactions, from flow acceleration around upstream turbines  
21 and from high speed turbulent structures in the on-coming fluid flow. Fur-  
22 thermore, these loads sources, as well as the effects of tidal cycles and turbine  
23 rotation, lead to a variety of cyclic loading events at various magnitudes and  
24 frequencies. In moving towards robust and cost effective designs, understand-  
25 ing and quantification of these loads will be required. It would seem pertinent  
26 to develop a series of standard load specifications under a number of oper-  
27 ational and environmental scenarios to which turbines can be designed and  
28 ultimately 'signed-off' against - similar to the IEC 61400 standard for the  
29 wind industry [5]. Although difficulties in adapting such an approach to the  
30 tidal industry surely exist, such a methodology will allow for increased load  
31 understanding, design maturity and improved turbine life expectancy fore-  
32 casting. Developments in the above are likely to bolster investor confidence  
33 and will aid in device underwriting by insurance companies - two important  
34 aspects that need to be addressed in order to create a functioning industry  
35 for the future.

36 This paper outlines the development process undertaken in designing and  
37 manufacturing three instrumented 1/20th scale HATT devices in order to  
38 understand the dynamic loading of HATTs, to inform developers and help

39 achieve survivability and efficiencies in the marine energy sector. The three  
40 devices have been manufactured and used for testing of HATTs singularly  
41 as well as in array configurations. In this way the impacts of array opera-  
42 tion and structure on turbine loading can be studied at scale. The paper  
43 describes the design specification, testing of the three HATTs at three sepa-  
44 rate test facilities (the Consiglio Nazionale delle Ricerche Institute of Marine  
45 Engineering (CNR-INM) wave-tow tank, the Institut Francais de Recherche  
46 pour l'exploitation de la mer (IFREMER) re-circulating flume and the Kelvin  
47 Hydrodynamic Laboratory (KHL) tow tank) to characterise each turbine in-  
48 dividually against the specifications. The individual data outputs were then  
49 compared to check for consistency. Initially the results relating to a sin-  
50 gle turbine undergoing testing at the CNR-INM facility are presented, this  
51 followed by a comparison of the outputs of the three turbines recorded at  
52 KHL. Lastly, a detailed analysis of the turbine performance at the IFRE-  
53 MER flume is presented considering the repeatability of the turbine mea-  
54 surements, the dimensional power and thrust performance, the drive shaft  
55 losses and Reynolds effects associated with turbine operation under low tur-  
56 bulence intensity flow regimes.

## 57 **2. A Review of Lab-Scale Turbine Testing and Design**

58 For the last 15-20 years, testing and development of scale model tur-  
59 bines has been utilised in both research and by turbine developers [6–12].  
60 Scale model testing has allowed developers to further understand design deci-  
61 sions during early Technology Readiness Levels (TRLs) with relatively small  
62 investments needed. In terms of research, the use of scale model HATTs

63 has proliferated and allowed researchers to understand the fundamental fluid  
64 dynamics, loading mechanisms and efficiencies associated with a variety of  
65 HATT rotor configurations. Furthermore, scale model testing has formed a  
66 vital part of using numerical modelling techniques to inform design modi-  
67 fications, both economically and relatively quickly, by providing validation  
68 data. Generally, scale testing to-date has proceeded at the 1/30th or higher  
69 depending on the size of the test facilities available for testing such devices.  
70 The use of nursery sites, however, has allowed for the development and test-  
71 ing of 1/5th scale devices - which is often a crucial step in moving towards  
72 a higher TRL full-scale deployments. As the turbine development detailed  
73 within this paper is specific to a 1/20th scale HATT this review section will  
74 be constrained to consider the form case exclusively.

75 In terms of first-hand experience gained by the authors, Cardiff Marine  
76 Energy Research Group (CMERG) has previously developed three working  
77 0.5 m diameter turbines. These have been used to conduct turbine design  
78 studies using CFD. Both turbines were developed using the HATT form.  
79 Details of the first turbine arrangement can be found in [13]. Testing with  
80 the first generation turbine was successful in validating and informing CFD  
81 models developed within the research group. The second generation lab-  
82 scale HATT was also developed, details of which are outlined in [14, 15].  
83 The turbine rotor and braking motor were directly coupled via a short drive  
84 shaft. This required that the motor was mounted inside the turbine housing,  
85 i.e. in the manner that is similar to many commercial turbine set ups with  
86 the motor taking the position of a Permanent Magnet Synchronous Machine  
87 (PMSM - typically used for direct drive applications). Thrust on the tur-

88 bine structure, including the stanchion was measured. This turbine was used  
89 extensively in studying the power converted and wake recovery associated  
90 with the rotor under plug flows, profiled flows, flow misalignment, wave cur-  
91 rent interaction and blade fault diagnostics Citations improved as suggested  
92 [13–18]. A third generation turbine was then designed within CMERG. The  
93 turbine was created using a similar rotor setup to the previous model scale  
94 allowing for both speed and torque control of the turbine. The turbine was  
95 fitted with a thrust and twisting moment transducer for a single blade, as  
96 well as an accelerometer housed in the nose cone. The rotor data captured  
97 was logged remotely via an Arduino mounted in the turbine nose cone. A  
98 similar stanchion arrangement was used to measure thrust loading on the  
99 turbine. The torque developed via the turbine rotor was measured via the  
100 integrated PMSM. This generation HATT was used for a variety of test cam-  
101 paigns studying turbine rotor faults, the effect of turbine yaw angle, wave  
102 loading effects and bend-twist coupling for blade load shedding Citations  
103 improved as suggested [13–19].

### 104 3. Blade Design

105 The blade, and ultimately the rotor, design of the detailed lab-scale device  
106 was developed to allow for adherence to Reynolds scaling and preservation  
107 of the Kinematic relationship between the blade tip speed relative to the  
108 incident fluid velocity. Details on the approach to Reynolds scaling can be  
109 found [20]. The Wortmann FX63-137 aerofoil has been used by CMERG for  
110 producing scaled HATT blades. Initially designed by Egarr [21], the blades  
111 have been extensively tested both numerically and experimentally [13], [15].

112 The aerofoil has high lift and low stall characteristics and a large root chord  
 113 length which aids a self starting capability [4]. An important aspect of the  
 114 design and development of the turbine was the development of an optimised  
 115 turbine rotor based on the Wortmann FX63-137 aerofoil. The chord lengths,  
 116 twist distribution from root to tip, pitch angle and hub attachment method  
 117 were all studied, with the goal of increasing the power coefficient,  $C_p$ , from  
 118 a peak of 0.4 while maintaining the thrust coefficient,  $C_T$ , to within 10% of  
 119 the levels observed in the previous blade geometry (i.e.  $C_T \approx 0.88$  at Peak  
 120  $C_P$  and  $\approx 0.99$  at freewheeling).

121 To aid the development of the rotor and turbine specification, the non-  
 122 dimensional coefficients have been utilised and defined by Equations 1 to 4,  
 123 below. Dimensional data have, however, been used where appropriate and  
 124 specified along with a reference fluid velocity.

$$C_P(\lambda) = \frac{Power}{0.5\rho AV^3} \quad (1)$$

$$C_\theta(\lambda) = \frac{Torque}{0.5\rho ARV^2} \quad (2)$$

$$C_t(\lambda) = \frac{Thrust}{0.5\rho AV^2} \quad (3)$$

125 where the tip speed ratio ( $\lambda$ ), is given as,

$$\lambda = \frac{\omega R}{V} \quad (4)$$

126 where,  $V$  is the fluid velocity in  $ms^{-1}$ ,  $\rho$  is the density of water in  $kg/m^3$ ,  
 127  $A$  is the turbine swept area in  $m^2$ ,  $R$  is the turbine radius in  $m$  and  $\omega$  is the

128 rotational velocity in  $rads^{-1}$ . The two methods used for the design develop-  
129 ment were Blade Element Momentum Theorem (BEMT) and Computational  
130 Fluid Dynamics (CFD).

131

### 132 3.1. Blade Element Momentum Theory

133 Optimising the blade design based on the Wortmann FX 63-137 profile  
134 was conducted in two stages: 1) the chord length distribution from blade  
135 root to tip and 2) the blade twist distribution. In total over 130 variations  
136 were considered using the University of Strathclyde BEMT code [22]. One of  
137 the main reasons for using BEMT initially is that the execution and compila-  
138 tion of the code is comparatively simple, when compared to other numerical  
139 methods and the blade design can be produced quickly, allowing for the ef-  
140 ficient study of a large number of blade geometry cases as required. The lift  
141 and drag coefficients for the Wortmann aerofoil were calculated using XFOIL.  
142 The  $C_P$  and  $C_T$  were compared for various chord length and twist distribu-  
143 tions. Those designs with the highest performance coefficients were plotted  
144 and the peak  $C_P$  was just over 0.45 at  $\lambda \approx 3.5$ , was found to be for a 19 deg  
145 twist, as show in 1.

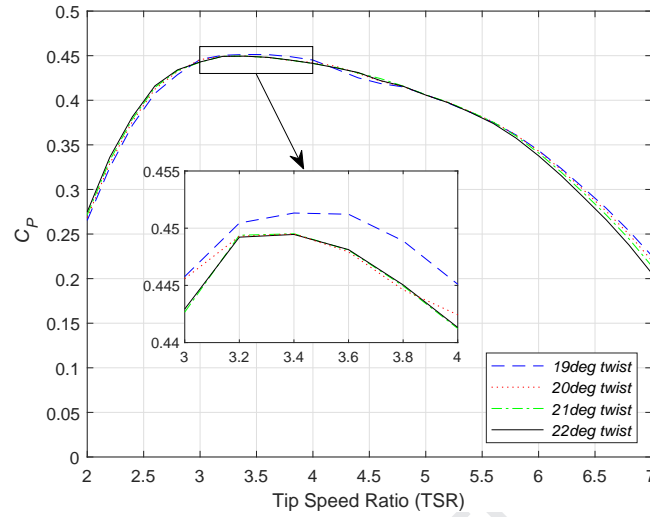


Figure 1: Comparison of the BEMT  $C_P$  predictions for twist distributions between 19-22 degrees

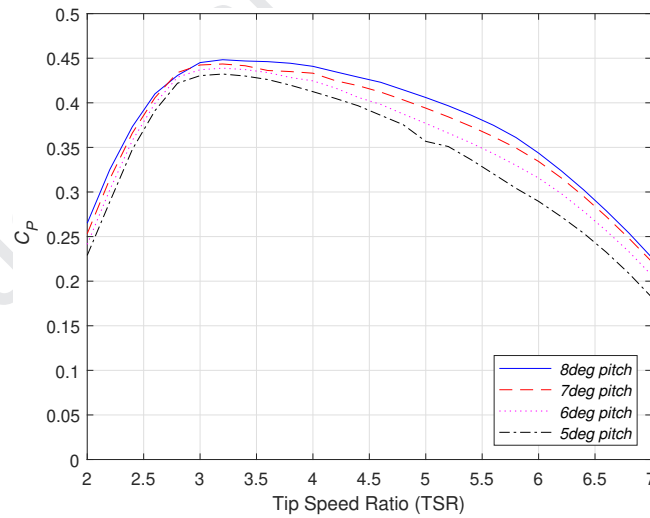


Figure 2: Comparison of the BEMT  $C_P$  predictions for pitch angles of 5-8 degrees

146 Finally a range of pitch angles between  $5^\circ - 8^\circ$  were studied in more  
 147 detail.  $C_P$  and  $C_T$ , for these pitch angles, can be seen in Figures 2 and 3,

148 respectively. The pitch angle of  $8^\circ$  was found to yield the highest  $C_P \approx 0.45$   
 149 with a  $C_T \approx 0.88$  at  $\lambda \approx 3.5$ .

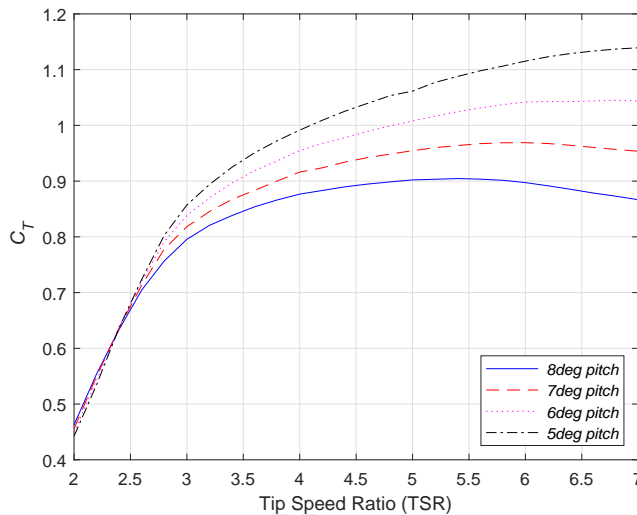


Figure 3: Comparison of the BEMT  $C_T$  predictions for pitch angles of 5-8 degrees.

### 150 3.2. Computational Fluid Dynamics

151 The optimised geometry, with a 384.5 mm blade length, was modelled  
 152 using ANSYS CFX. Approximately, 60 mm length of the blade, from the  
 153 root, was modified and blended with the Wortmann profile to enable the  
 154 blade to be connected to the turbine hub. The models developed all contained  
 155 a Moving Reference Frame (MRF), as sub domain which encompassed the  
 156 entire turbine rotor. The inclusion of the MRF facilitated simulation of the  
 157 turbine rotation. The width, depth and height of the overall fluid domains  
 158 were generated to replicate the geometries of the test facilities ultimately  
 159 used for turbine characterisation.

160 An outline of the CFD models are presented here, with details presented  
 161 in Table 1. However, further details can be found in [23]. Each blade was

162 divided into three sections: the blade tip, middle and root. The smallest  
 163 elements were concentrated at the tip, starting at 3 mm gradually increasing  
 164 to 7 mm at the root and hub. The growth rate, specifying the rate of cell size  
 165 growth, was set to 1.1, with the maximum element size set to 20 mm, which  
 166 resulted in 3 million elements, with around half of these elements contained  
 167 within the MRF. A  $1 \text{ ms}^{-1}$  plug flow boundary condition was applied to the  
 168 inlet of the model domain and a static pressure of 0 Pa at the outlet. The  
 169 walls, base, faces of turbine, hub and stanchion were all set to the no slip  
 170 condition with the top of the domain defined as an opening. **The RANS**  
 171 **equations were closed using the SST  $k\text{-}\omega$  turbulence model as developed by**  
 172 [24] and successfully applied to tidal turbine modelling in [13, 15, 16, 20].  
 173 A comparison made between the torque and thrust results from the steady  
 174 state and transient models showed less than 2% differences hence the steady  
 175 state model was used to reduce modelling time.

Table 1: CFD modelling information

Model Name		No Stanchion	CNR-INM	IFREMER
Geometry	Domain	6[m] x 6[m] x 11[m]	9[m] x 3.5[m] x 20[m]	4[m] x 2[m] x 18[m]
	Dimensions			
	Stanchion	No	Yes	Yes
Set Up	Inlet	1[m/s]	1[m/s]	1.1[m/s]
	Outlet	Pressure 0[Pa]	Pressure 0[Pa]	Pressure 0[Pa]
	Walls	Free Slip	No Slip	No Slip
	Top	Free Slip	Opening	Opening
	Solver Type	Steady	Steady	Steady

176 The results from the CFD modelling along with the BEMT results are  
 177 presented in Figures 6 and 7. By comparing the BEMT to the CFD model  
 178 that includes the stanchion it can be seen that the BEMT generates higher  
 179 predictions for both the  $C_P$  and  $C_T$ , due to the stanchion not being taken into  
 180 consideration as part of the BEMT calculation. The flow directly behind the  
 181 blades will have a lower velocity due to the blockage effect of the stanchion  
 182 and ultimately reduce the performance of the blade passing the stanchion  
 183 [15]. If the stanchion is removed from the CFD model and compared with  
 184 the BEMT results, then a much closer comparison between both the thrust  
 185 and the power can be seen. The BEMT results also showed a lower  $\lambda$  value for  
 186 peak power. The authors suggest that this may be due to Reynolds effects  
 187 in matching the lift and drag coefficients, similar findings were presented in  
 188 [25].

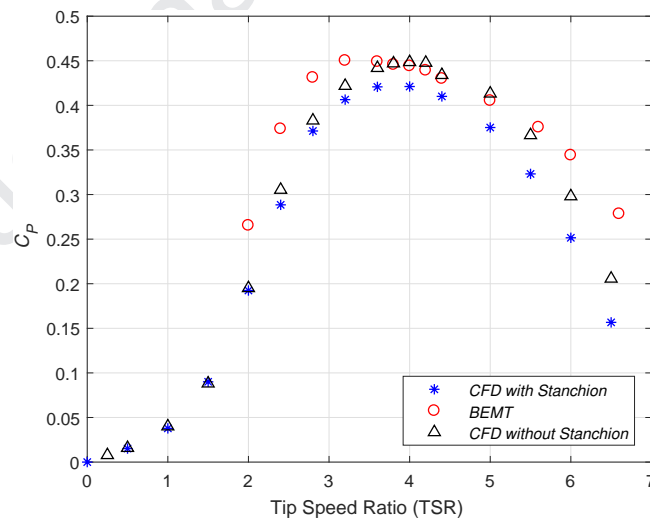


Figure 4: Comparison of the  $C_P$  between CFD and BEMT

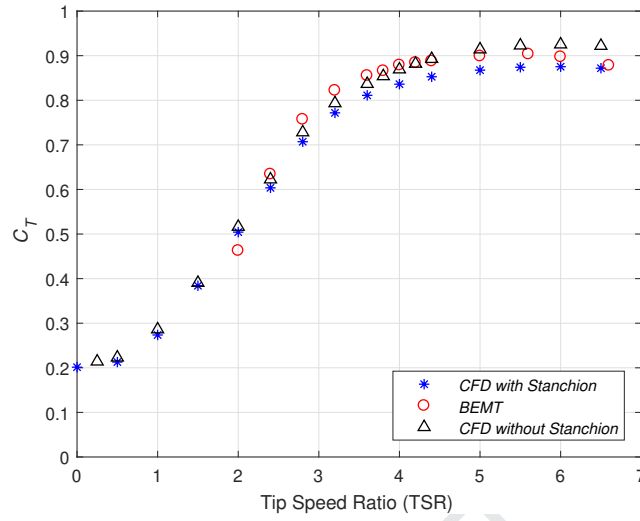


Figure 5: Comparison of the  $C_T$  between CFD and BEMT

Table 2: Overview of new rotor ( $D = 0.9m$ ) parameters used to develop the design specification.

Quantity	Rotor Value
Peak $C_P$	0.42 ( $\lambda \approx 4.0$ )
Peak $C_T$	0.88 ( $\lambda \approx 6.0$ )
Peak $C_q$	0.14 ( $\lambda \approx 2.0$ )
Freewheeling	$\lambda = 8$
Peak Power	293 W (110RPM)
Peak Thrust ( $U = 1.3ms^{-1}$ )	615 N (165RPM)
Peak Torque ( $U = 1.3ms^{-1}$ )	44 Nm (55RPM)
Max RPM at $1.3ms^{-1}$	220

## 189 4. Turbine Design

190 The following section details the design of the nacelle, drive train, elec-  
191 tronic machine and instrumentation generated to compliment the newly de-  
192 veloped blades forming a 1/20th instrumented HATT. The section is split  
193 into two parts. The first focusses on the design requirements for the turbine  
194 development and the second details the design solution developed to meet  
195 the outlined requirements.

### 196 4.1. Design Criteria

197 The specifications for the turbines are shown in Table 3A. The  $C_T$  and  
198  $C_P$  for the rotor geometry were used to develop the rated loadings and power  
199 output for the HATT design. As the CFD results hadn't been validated at  
200 this stage, a safety factor of 1.5 was applied to the rated quantities, at a  
201 mean flow velocity of  $1.3 \text{ ms}^{-1}$  and instantaneous velocities up to  $1.5 \text{ ms}^{-1}$   
202 (based on a turbulence intensity of 15%). This corresponds to a mean chord  
203 based Reynolds number,  $RE_{0.7Chord} = 8.44E + 4$  as defined in Appendix A.  
204 The design loads were based on the standard equations defined in Equations  
205 1 to 4.

Table 3: Table outlining the main design specifications and Instrumentation List for the developed HATT.

**A.**

Requirements List	
Specification	Details
Rated Flow Velocity	Continuous: $1.3 \text{ ms}^{-1}$ Instantaneous: $1.5 \text{ ms}^{-1}$
Rated Power	0.6 kW
Maximum Rotational Velocity	350 RPM
Rated Torque	Continuous: 41 Nm Instantaneous: 54 Nm
Maximum Rotor Thrust	1.07 kN
Maximum Blade Root Bending Moment	Flapwise: 129.76 Nm Edgewise: 18.13 Nm
Sample Rate Load Measurements	1032 Hz
Control Types	Speed Control (SC), Torque Control (TC) Regulated Torque Control Optimal $\lambda$ control

**B.**

Instrumentation List
Flap-wise and Edge-wise blade root bending moments (each blade); Rotor Thrust; Rotor Torque; Rotor Position; Rotational Velocity; PMSM Torque; Stanchion Bending Moment; Support Structure Vibration.

206 The diameter of the turbine was specified as 0.9m, this was in line with a  
207 1/20th scale HATT. A direct-drive device was decided upon, this was based  
208 upon the experience acquired during development of the legacy HATTs de-  
209 veloped by the authors and detailed in [14]. The turbine control and power  
210 take-off were to be undertaken by a PMSM. The power flow from the tur-  
211 bine and its associated braking torque were to be controlled by a drive series  
212 made up of back-to-back Voltage Source Converters (VSCs) either side of a  
213 DC bus. This decision was made based on the flexibility demonstrated when  
214 previously using such a set up. Previously closed-loop, set-point speed and  
215 torque control had been demonstrated. Furthermore, with the addition of  
216 outer control loops this set up could be utilised to achieve optimal power  
217 and torque control strategies allowing for more focused research into turbine  
218 loadings under representative control scenarios[26].

219 As the primary aim of the scale model HATT was for use in studying  
220 dynamic and transient loading characteristics, rotor load measuring instru-  
221 mentation was to be included. This ensured that the turbine was capable of  
222 providing dynamic,  $C_P$ ,  $C_T$  and  $C_\theta$  measurements directly associated with the  
223 turbine rotor. To compliment this the capability of measuring the dynamic  
224 blade root bending moments, for each turbine blade, was incorporated. To  
225 allow for the high fidelity study of transient loading throughout a turbine ro-  
226 tation, sample rates were required such that one sample per  $2^\circ$  was collected  
227 at turbine free-wheeling for the rated fluid velocity of  $1.3 \text{ ms}^{-1}$ . Based on  
228 the power curves developed via CFD, free-wheeling was found to occur at,  
229  $\lambda \approx 8$ . At  $1.3 \text{ ms}^{-1}$  this corresponds to a free-wheeling rotational velocity of  
230 220 RPM or a sampling rate of 1324 Hz to fulfil the stipulated requirement.

231 Lastly, the requirement was stipulated of a maximum measurement uncer-  
232 tainty (for each instrument) of 5 % of the maximum loads measured for each  
233 instrument.

#### 234 *4.2. Design Overview*

235 A cross section of the turbine can be seen in the rendered SolidWorks  
236 image shown in Figure 6. The HATT power transfer mechanism utilises a  
237 direct-drive set-up with turbine control and power take-off undertaken by a  
238 Permanent Magnet Synchronous Machine (PMSM) controlled via back-to-  
239 back VSCs. The front section of the turbine was developed to house an  
240 instrumentation suite consisting of an integrated rotor thrust/torque trans-  
241 ducer, an encoder and an instrumented rotor. The instrumented rotor was  
242 developed to measure, 'flap-wise' and 'edge-wise' blade root bending mo-  
243 ments for each turbine blade.

244 Additional installed instrumentation includes a moisture sensor, stan-  
245 chion bending moment measurements and support structure vibration mea-  
246 surements. The instrumentation wiring is transferred into the rotational  
247 reference frame by an 18-way slip ring mounted on the turbine drive shaft.  
248 The turbine body is flanged together with the support stanchion through  
249 which the power, encoder and instrumentation cables are fed.

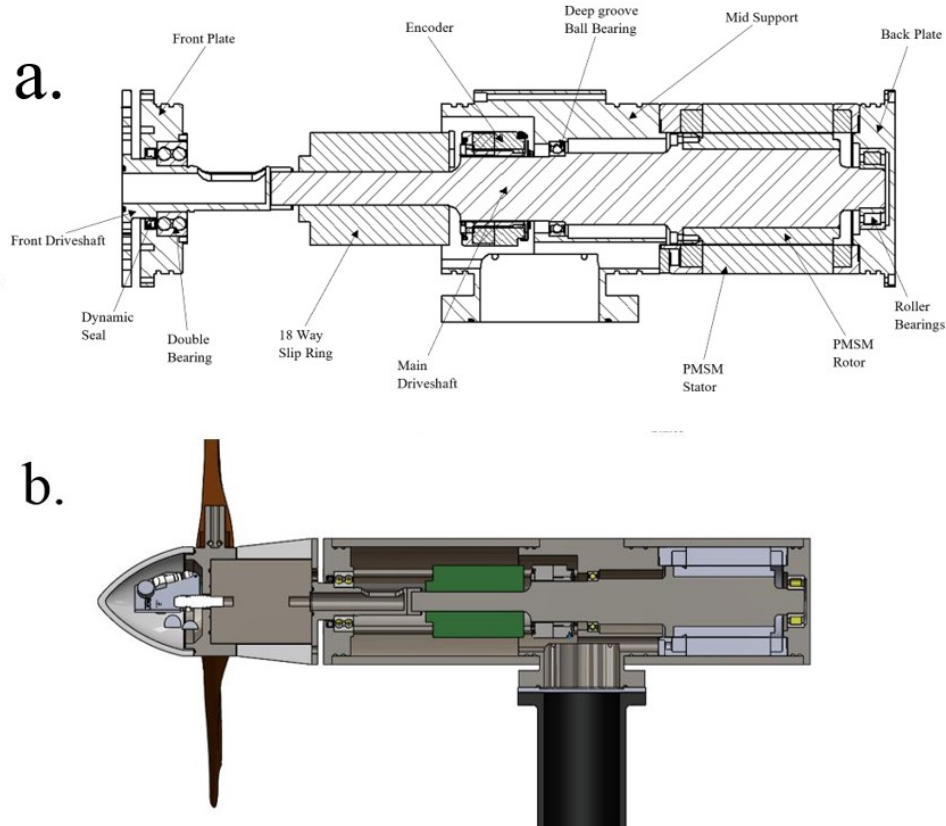


Figure 6: Solidworks rendering of the 1/20th scale HATT.

#### 250 4.3. Drive Train Design

251 The turbine was designed as a direct drive HATT. As shown in Figure  
 252 6, it was created via two drive interfacing shafts to allow for the flanging  
 253 arrangement to the thrust/torque transducer. Using two drive shafts also fa-  
 254 cilitated the positioning of the PMSM on back side of the turbine away from  
 255 the rotor instrumentation. The structure of the design was created to intro-  
 256 duce modularity into the design to allow for instrumentation developments  
 257 and ease of part replacement. The design decision to position the PMSM at

258 the back end of the HATT was also undertaken to reduce electrical noise in  
259 the measurement readings.

260 The drive shaft was supported by three bearing housings; the mid sup-  
261 port, front and back plates. The first shaft has a hollowed section to accom-  
262 modate instrumentation cabling, which was fed from the rotating portion of  
263 the 18-way slip ring. The front shaft was supported by double row bearings,  
264 which act as the main thrust bearing and are housed in the front plate. A  
265 dynamic seal was embedded in the front plate to protect from water ingress.

266 The main drive shaft was supported in two places, at the mid support and  
267 back plate. The front and back drive shafts are coupled together to transfer  
268 torsional loads and rotational motion. The main shaft has been fitted with  
269 an encoder and slip ring to the left of the mid plate and a PMSM to the right  
270 of the mid plate with respect to Figure 6.

#### 271 *4.4. Permanent Magnet Synchronous Machine, Drives and Control*

272 The model scale HATT houses an embedded PMSM for turbine breaking  
273 and control. The PMSM used was a Bosch Rexroth MST 130E. The ratings of  
274 the motor are presented in Table 4. The motor was chosen for its relative high  
275 torque capacity for a non-directly cooled motor as required by the direct-drive  
276 configuration. The rotor of the PMSM houses permanent magnets arranged  
277 into 10 pole pairs and was mounted on the back drive shaft fastened via a  
278 flange. The stator contains the motor windings and was integrated via the  
279 mid-section and back plates of the HATT. To cool the motor appropriately,  
280 the motor was aligned and fitted into the stainless steel nacelle of the HATT.  
281 Circular steps on the mid-section and back plate align the stator relative to  
282 the drive shaft to preserve the air gap of 0.4 mm.

283 Power flow to and from the PMSM was managed by a drive section,  
284 which was located in a cooled drive cabinet. The drive sections are made  
285 up of a mains choke, a mains filter, a rectifier and an inverter. A three  
286 phase connection was made to the mains choke which manages regenerative  
287 energy feedback into the grid when required. The three phase connection  
288 was the made between the mains choke and the mains filter, filtering was  
289 undertaken to maintain power quality in the supply to the rectifier. The  
290 filtered three phase connection was then fed to a rectifier where the AC  
291 current was converter to DC via a VSC with a switching frequency of 4000  
292 Hz. The rectifier and inverter are connected via a DC bus integrated with  
293 a DC bus capacitor. The inverter then creates a three phase AC current  
294 which was connected to the motor. The power flow to and from the motor  
295 are managed by the VSCs either side of the DC bus - similar to back-to-back  
296 set up used for HATTs and wind turbines adopting a direct-drive PMSM  
297 topology. The back-to-back VSCs allow for servo based Vector Oriented  
298 control of the turbine to directly the torque required of the PMSM or via an  
299 additional velocity control loop the desired rotational velocity. The encoder  
300 required for servo-control of the PMSM is detailed in [Section 4.5.3](#).

#### 301 *4.5. Instrumentation*

302 An instrumentation suite was integrated into the turbine in order to quan-  
303 tify dynamic loadings on the HATT under various fluid flow regimes. An  
304 overview of the instrumentation suite integrated into the turbine is presented  
305 below.

Table 4: The motor parameters for the Bosch Rexroth MST130E.

<b>Motor Parameters</b>	
Rated Torque	42 Nm
Maximum Speed	350 RPM
Rated Power	0.6 kW
Maximum Rotational Velocity	350 RPM
No. of Pole Pairs	10
Winding Resistance	14.9 $\Omega$
Mass of Stator	7.7 kg
Mass of Rotor	2.2 kg

#### 306 4.5.1. Rotor Torque and Thrust Transducer

307 A bespoke rotor torque and thrust transducer was created by Applied  
308 measurements Ltd. The transducer used was an adapted DBBSS/TSF Torque  
309 and Axial Force Sensor, which had a rated maximum thrust load of 1.8 kN  
310 and a maximum rated torsional loading of 100 Nm. The transducer was  
311 adapted for the specified load rating, for waterproofing, to house two 18 way  
312 Lemo EGG.2B.318 connectors and to accommodate through wiring for hub  
313 instrumentation. The transducer was fastened between the front drive shaft  
314 and the turbine rotor upstream of any bearings or seals to measure rotor  
315 loads prior to any drive shaft losses. The transducer used two ICA4H am-  
316 plifiers, one for thrust loading with a sensitivity of 0.005 mA/N and one for  
317 torque loading with a sensitivity of 0.08 mA/N, both amplifiers were housed  
318 in the body of the transducer.

#### 319 *4.5.2. Instrumented Hub*

320 The turbine hub was created to house the blades and measure both flap-  
321 wise and edge-wise bending moments on each of the three turbine blades.  
322 The hub is a circular section with holes for flange fixing to the thrust/torque  
323 transducer, a bore in the centre accommodates a Lemo connector for instru-  
324 mentation wiring. Three 'bosses' project radially from the outside of the  
325 circular section, to which the blades are attached via grub screws. Each of  
326 the bosses were spaced at  $120^\circ$  and each of the bosses houses two full-bridge  
327 strain gauge set ups for measuring blade root bending moments.

328 The boss sizes were set such that they limited the stress on the machined  
329 faces to 30% of the material yield stress, whilst setting a suitable strain level  
330 on the faces.

#### 331 *4.5.3. Encoder*

332 The encoder selected, and used for position feedback, was an optical en-  
333 coder, the model utilised was the Heidenhain ENC113 encoder with Endat  
334 2.2 interfacing. The encoder is of 13 bit type with a quoted system accuracy  
335 of  $\pm 20$  seconds of arc.

#### 336 *4.5.4. Amplification and Signal Processing*

337 The blade load and thrust/torque transducer measurements all utilised in-  
338 tegrated circuit ICA4H amplifiers. The output of the amplifiers was between  
339 4 mA and 20 mA and can accommodate bridge systems with sensitivities be-  
340 tween 0.5 mV/V and 150 mV/V. A gain setting resistor was used to achieve  
341 measurements in the 4 mA to 20 mA range for differing bridge sensitivities.  
342 The amplifier required 24 V input and outputs a regulated 5 V supply to

343 the wheatstone bridge configurations. The amplifier has an inbuilt low-pass  
344 filter with a fixed cut-off frequency of 1 kHz.

345 The stanchion bending moment instrumentation, consisting of a full-  
346 bridge configuration of strain gauges, was amplified and filtered by a PCM  
347 Strain Gauge Amplifier(SGA). The PCM SGA was set to filter the amplifier  
348 output at 1 kHz. Lastly, the piezo-electric vibration sensors signals are not  
349 amplified and are filtered at the NI9234 DAQ card by a low pass filter with  
350 the cut-off frequency set to set to 5kHz. The low pass filters cut-off values  
351 are set to act as an anti-aliasing filter to ensure quality of transient analysis  
352 of the captured loading and vibration data. Table 5 shows the sample rate  
353 and anti-aliasing filter cut-off frequency for each piece of instrumentation.

#### 354 *4.5.5. Data Acquisition*

355 Data acquisition for all three turbines was undertaken via a National  
356 Instruments Compact RIO. The DAQ cards used in the compact RIO are  
357 outlined in Table 5. The table shows the measurement type, bit depth, sam-  
358 ple rate and anti-aliasing filter cut-off frequency for each of the channels. A  
359 Compact RIO was utilised due to the advantages of being able to utilise both  
360 the Field Programmable Gate Array (FPGA) and the Real-Time operating  
361 system for test control and data capture and management. The tasks under-  
362 taken by the Compact RIO have been broadly split into data capture and  
363 triggering, which was undertaken by the FPGA and data management and  
364 test control which was undertaken by the Real-Time operating system.

Table 5: Table outlining the NI DAQ cards used for data capture along with information on the measurement type, bit depth, sample rate and anti-aliasing filter cut-off frequency.

Measurement Type	DAQ Card	Bit Depth	Sample Rate	Low Pass Cut-off
Blade root bending moment	NI9203	16-Bit, 0-20 mA	2 kHz	1 kHz
Rotor Thrust	NI9203	16-Bit, 0-20 mA	2 kHz	1 kHz
Rotor Torque	NI9203	16-Bit, 0-20 mA	2 kHz	1 kHz
Stanchion Bending Moment	NI9207	24-Bit, 0-10 V	2 kHz	1 kHz
Stanchion Vibration	NI9234	24-Bit, 0-100 mV	10 kHz	5 kHz

#### 365 4.6. Waterproofing and Moisture Sensor

366 Figure 7 shows an overview of the sealing arrangement for the main tur-  
 367 bine assembly. Generally, sealing of the turbine was accomplished using O-  
 368 rings, with O-ring sizing and groove specification undertaken following the  
 369 BSI 4518 British standard. As mentioned a dynamic seal was utilised to  
 370 seal around the entry point of the front drive shaft into the turbine nacelle  
 371 through the front plate.

372 An interlock moisture sensor was integrated into the turbine to alert the  
 373 user in the event that any of the outlined sealing arrangements failed and  
 374 water ingress into the turbine occurred. This feature was required for both  
 375 safety and to protect the scale model HATT hardware. The circuit was  
 376 connected to 10 V source, output from the Compact RIO; in the event of  
 377 water ingress the two moisture probes are shorted or connected together.  
 378 The shorting of the two probes changes the circuit output from 10 V to 0V  
 379 (ground). A 0 V reading from the moisture sensor then starts an automatic

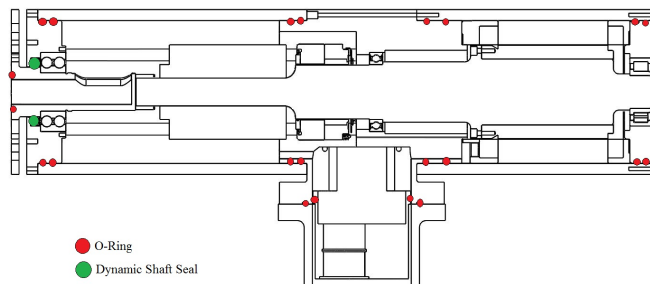


Figure 7: Overview of the sealing arrangements for the 1/20th Scale HATT.

380 shut down of the turbine PMSM to avoid any electrical damage. Lastly, the  
 381 user would be alerted of the leak so the turbine can be removed from the tow  
 382 tank or flume.

### 383 5. Turbine Characterisation Testing

384 Initially, a single turbine, Turbine T1, was manufactured and tested.  
 385 Once this turbine was validated in terms of design and operation the fur-  
 386 ther two turbines, T2 and T3, were constructed. As such, turbine testing  
 387 was conducted in 3 stages:

388 **Stage 1:** Testing undertaken to provide validation of the design and  
 389 characterisation data for a single turbine over the full working  $\lambda$  range. This  
 390 testing, funded by Marinet 2, was undertaken at the CNR-INM wave-tow  
 391 tank in Rome, Italy. This allowed for characterisation of the turbine with  
 392 and without defined waves at controlled speeds with no turbulence present.  
 393 In addition, testing of the turbine's ability to operate under speed or torque  
 394 control was conducted.

395 **Stage 2:** The single turbine was then tested in the IFREMER wave-  
 396 current flume facility in Boulogne-Sur-Mer, France, again with and without

397 waves. This allowed for a low turbulence level and a range of flow speeds,  
398 again over the full  $\lambda$  range.

399 **Stage 3:** With the turbine design validated, the second and third turbines  
400 were manufactured and tested in the Kelvin Hydrodynamics Laboratory  
401 (KHL) tow tank, in Glasgow.

402 Table 6 shows an overview of the experimental parameters for each facility.  
403 It should be noted that differing pitch angles were used for the IFREMER  
404 and KHL cases, this was done to test the effects of differing pitch angles and  
405 to understand the repeatability of the pitch angle setting procedure.

Table 6: Table providing an overview of peak non-dimensional quantities observed across the differing test facilities for Turbine 1 (T1).

<b>Qty</b>	<b>CNR-INM</b>	<b>IFR</b>	<b>KHL</b>
Facility Type	Tow Tank	Flume Tank	Tow Tank
Testing Data	November 2017	April 2018	February 2019
Data Record Length	90s	100s	60s
Facility Dimensions	$9 \times 3.5 \times 220$ m	$4 \times 2 \times 14$ m	$4.6 \times 2 \times 76$ m
Blockage Ratio	2.8 %	8.0 %	6.9 %
Turbine Depth	1.5 m	1 m	1 m
Pitch Angle	$8.0^\circ$	$6.2^\circ$	$6.2^\circ$
Flow/ Carriage Velocities	$1.00 \text{ ms}^{-1}$	$0.50 \text{ ms}^{-1}$ $0.60 \text{ ms}^{-1}$ $0.90 \text{ ms}^{-1}$ $1.00 \text{ ms}^{-1}$ $1.05 \text{ ms}^{-1}$ $1.10 \text{ ms}^{-1}$ $1.20 \text{ ms}^{-1}$ $1.30 \text{ ms}^{-1}$	$0.80 \text{ ms}^{-1}$ $1.0 \text{ ms}^{-1}$ $1.2 \text{ ms}^{-1}$

406 *5.1. CNR-INM Testing*

407 The Stage 1 tests were undertaken at the CNR-INM wave tank. The  
408 tests were conducted by attaching the model HATT to the carriage and  
409 towing it along the tank as shown in Figure 8A. The tests were undertaken to  
410 characterise the HATT and to confirm its correct operation. A series of tests  
411 were undertaken all with the carriage velocity set to  $1 \text{ ms}^{-1}$  ( $RE_{0.7chord} =$

412  $6.48 \times 10^4$ ). A 0.09 m diameter stanchion held the turbine in place to the  
413 tow carriage. The turbine hub centre was set at 1.5 m below the still water  
414 surface, and centred in the cross-stream direction. Cables from the turbine  
415 were run inside the stanchion to the control and data acquisition systems  
416 situated on the carriage. For this set of tests the pitch angle for each blade  
417 was set to  $8^\circ \pm 0.5^\circ$ . The tests were undertaken with both speed and torque  
418 control over the range of operating  $\lambda$  values. Prior to each test a zero reading  
419 was taken to confirm no drift in the instrumentation had occurred.

#### 420 5.2. IFREMER Testing

421 The Stage 2 test campaign was undertaken at the flume tank facility in  
422 Bolougne-Sur-Mer in France. Again a major aspect of this testing was to  
423 characterise the turbine performance. In this instance the turbine blades  
424 were set to a pitch angle of  $6.2^\circ \pm 0.5^\circ$ . The turbine was supported via the  
425 same stanchion arrangement as the CNR-INM testing described in Section  
426 5.1, albeit with different supporting bracket arrangement. The setup can be  
427 seen in Figure 8B. The turbine in this case was submerged to a depth of 1 m  
428 meter and again centralised in the cross stream direction. A Laser Doppler  
429 Velocimeter (LDV) was setup to measure the fluid velocity in the stream-  
430 wise and cross-stream directions. The measurement volume of the LDV was  
431 aligned with the centre of the turbine nose cone, 1 m upstream.

432 In this instance the turbine was characterised under a variety of fluid  
433 velocities ranging between  $0.5 \text{ m s}^{-1}$  ( $Re_{0.7Chord} = 3.25 \times 10^4$ ) and  $1.3 \text{ m s}^{-1}$   
434 ( $Re_{0.7Chord} = 8.44 \times 10^4$ ). A honeycomb flow straightener was used at the  
435 flow inlet to straighten the flow and reduce the turbulence levels, with prior  
436 characterisation of the fluid flow under this set up finding turbulence intensi-

437 ties of approximately 2%. Similarly to the testing undertaken at CNR-INM,  
438 both speed and torque control methods were utilised with a variety of rota-  
439 tional velocities and feedback torques applied to test the turbine at a variety  
440 of  $\lambda$  values.

### 441 5.3. Kelvin Hydrodynamics Laboratory testing

442 Stage 3 testing was undertaken at the Kelvin Hydrodynamic laboratory,  
443 the turbine set-up prior to lowering to the 1 metre depth can be seen in  
444 Figure 8C. The tests were undertaken to individually characterise the three  
445 HATTs, to confirm their correct operation and provide a comparison with  
446 each other. An initial series of tests were undertaken for 8  $\lambda$  settings with  
447 carriage speeds of 0.8, 1.0 and 1.2  $m s^{-1}$  ( $Re_{0.7Chord} = 5.184 \times 10^4$ ,  $6.48 \times 10^4$   
448 and  $7.76 \times 10^4$  respectively), with speed control. The turbine hub centre  
449 was set 1.0 m below the still water surface and centred in the cross-stream  
450 direction. Cables, were again, run along the inside of the stanchion from the  
451 turbines and connected to the control and data acquisition systems situated  
452 on the carriage. For this set of tests the pitch angle for each blade was set  
453 to  $6.2^\circ \pm 0.5^\circ$ . On completion of the speed control experiments a series of  
454 tests were then completed using torque control. As with all tow tank testing  
455 described in this paper prior to each, for each turbine, a zero reading test  
456 was undertaken to confirm no drift in the instrumentation had occurred.

### 457 5.4. Results

458 The results section presents the data recorded during the aforementioned  
459 testing campaigns with a focus on two aspects: the characterisation of turbine  
460 T1 during testing at three differing facilities, Section 5.4.1, and a comparison

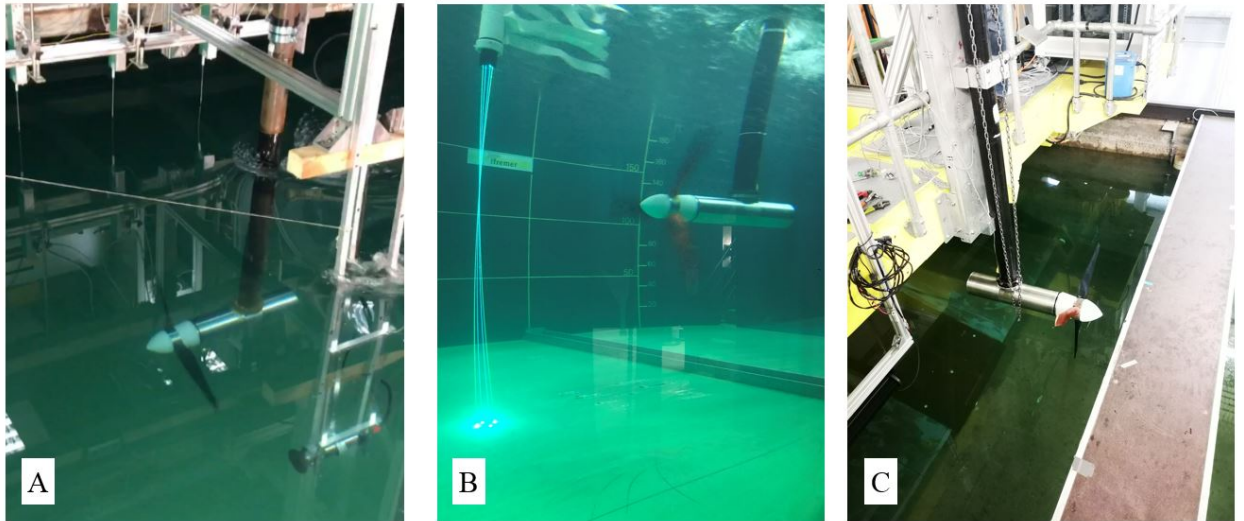


Figure 8: The test setups at the various testing facilities, A) CNR-INM, B) IFREMER and C) KHL.

461 between the results obtained for each of the three turbines tested at KHL,  
 462 Section 5.4.2.

#### 463 5.4.1. Single Turbine Calibrations

464 Figures 9 and 10 show a comparison between the results obtained dur-  
 465 ing the CNR-INM, IFREMER and KHL test campaigns for turbine T1 and  
 466 a flow velocity of  $1 \text{ ms}^{-1}$ . A comparison was made between the raw and  
 467 non-dimensional analogues of the power, torque and thrust developed by the  
 468 turbine. Data for both speed and torque control strategies have also been  
 469 included for the test campaigns undertaken at both CNR-INM and IFRE-  
 470 MER. The non-dimensional coefficients were calculated using equations 1 to  
 471 4. Power and torque, along with the non-dimensional equivalents, were cal-  
 472 culated for this comparison using the measured PMSM winding currents, as

473 the rotor torque transducer was not available during the CNR-INM testing  
474 campaign. The PMSM winding current measurements were decomposed into  
475 direct and quadrature axis currents, the quadrature axis currents were then  
476 scaled to give the braking torque applied by the PMSM - in this regard it  
477 should be noted that these measurements included drive shaft losses. In the  
478 cases of the CNR-INM and KHL facilities, the fluid velocity used in the cal-  
479 culations was the carriage velocity. In the case of the IFREMER testing, the  
480 fluid velocity used to calculate the non-dimensional power coefficients was  
481 the swept-area averaged fluid velocity.

482 As the differing facilities had differing cross-sectional areas, see Table  
483 6, flow around the turbine would have been constrained and accelerated to  
484 differing degrees, resulting in artificially exaggerated turbine performances  
485 being recorded. As such, the non-dimensional parameters were corrected to  
486 account for the differing blockage ratios in the differing facilities. This was  
487 done by estimating the ratio of blockage constrained flow velocity to open  
488 channel flow velocity,  $U/U_f$ , using the method detailed in [6]. The ratios  
489 developed are plotted in Figure 9 against  $\lambda$  values for the differing facilities.  
490 The aforementioned ratio was squared and cubed before applying as a factor  
491 to the non-dimensional thrust and power coefficients, respectively. Table 7  
492 shows the peak non-dimensional values obtained for turbine T1 during the  
493 three stages of testing described.

494

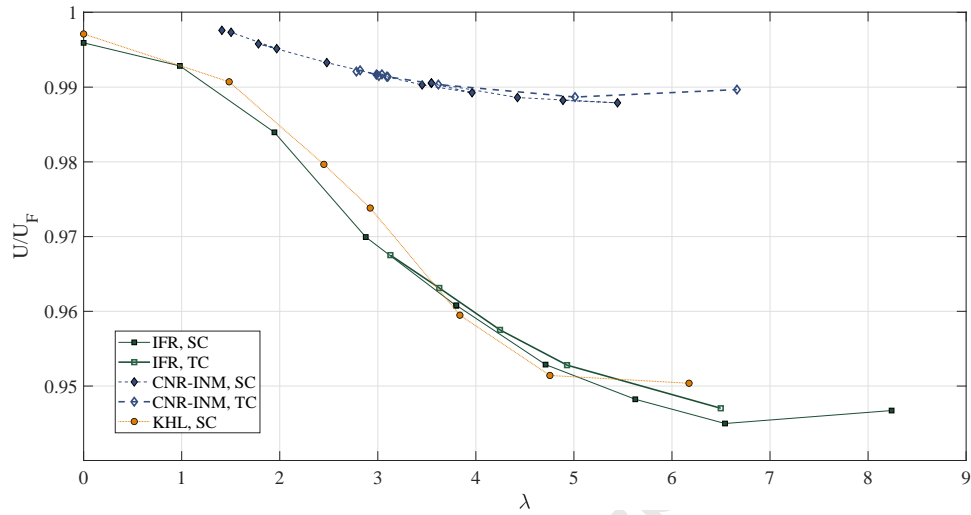


Figure 9: The blockage ratio of constrained flow to open channel flow velocity,  $U/U_f$ , against  $\lambda$  values for the three differing test facilities.

Table 7: Table providing an overview of peak, blockage corrected non-dimensional quantities observed across the differing test facilities for Turbine 1 (T1).

Qty	CNR-INM	IFR	KHL
Max $C_P$	0.38	0.35	0.37
$\lambda$ @ Max $C_P$	3.55	3.13	2.92
Max $C_\theta$	0.134	0.119	0.141
$\lambda$ @ Max $C_\theta$	2.5	2.9	2.5
Max $C_T$	0.86	0.94	0.94
$\lambda$ @ Max $C_T$	5.5	6.5	6.2

495 Table 7 shows that relatively good agreement was found in the maximum  
 496 power, torque and thrust coefficients measured. However, it should be noted  
 497 that a lower power coefficient was recorded for the IFREMER test cases,

498 as well as discrepancies in the  $\lambda$  values recorded for peak power. Further  
 499 to this, a slightly lower  $C_\theta$  value was also recorded for the IFREMER test  
 500 case. Better agreement was seen in the  $\lambda$  value of peak torque coefficient. A  
 501 lower value of thrust coefficient was observed, as expected, for the CNR-INM  
 502 testing. This was likely due to the differing pitch angle setting for the CNR-  
 503 INM test and helps confirm that in the region of pitch angles varying between  
 504  $6^\circ$  and  $9^\circ$  a greater sensitivity in thrust loading is observed in contrast to a  
 505 relatively invariant power coefficient, as discussed in Section 3.

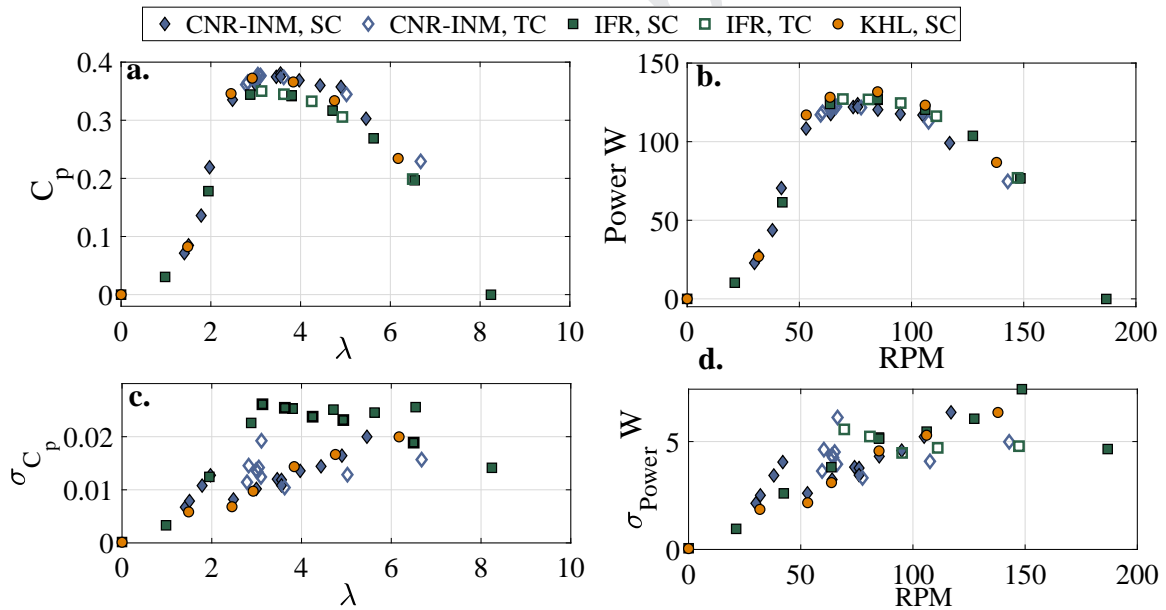


Figure 10: Blockage corrected power curves obtained whilst testing at CNR-INM, IFREMER and KHL. a) Shows Non-Dimensional power coefficient against  $\lambda$ . b) Shows Power against RPM. c) Shows the standard deviation in non-dimensional power coefficient against  $\lambda$ . d) Shows the standard deviation of power against RPM.

506 Inspection of the power curves, in Figure 10, shows that the IFREMER  
 507 test cases yielded a generally lower performance curve than the CNR-INM

508 and KHL test cases. Comparison of Figures 10a and 10b shows the block-  
 509 age correction has a significant effect. Whilst the highest power capture was  
 510 observed for the KHL cases, the blockage correction yields  $C_P$ -curves of a  
 511 similar level for the CNR-INM and KHL cases. The discrepancy between  
 512 the IFREMER  $C_P$ -curve and CNR-INM and KHL  $C_P$ -curves is likely to be  
 513 due to greater drive-train losses during the IFREMER test. A change of  
 514 dynamic seal between the CNR-INM and IFREMER testing campaigns was  
 515 undertaken which could explain the deviation. Furthermore, it is also possi-  
 516 ble that the change in the losses across the differing facilities may have altered  
 517 the power capture to thrust relationship exploited in the blockage correction  
 518 approach. This may have led to a distortion in the blockage correction factor  
 519 applied in the case of the IFREMER tests.

520 It can be seen in Table 7 that the  $\lambda$ -value associated with maximum power  
 521 performance varies between facilities - this is likely to be a result of the  $C_P$ -  
 522 curve shape than any inherent difference between the facilities. Explicitly,  
 523 this is due to the relatively flat shape of the characteristic  $C_P$  curve in the  
 524 peak region as shown in Figure 10a. This may have been exacerbated by the  
 525 differing  $\lambda$  values tested for each of the differing test campaigns.

526 The maximum standard deviation of power and  $C_P$  were of the order of  
 527 3 and 3.5 % of the mean values obtained, respectively. The variability of the  
 528 power produced by the turbine generally increased with rotational velocity  
 529 as shown in Figures 10c and 10d. The dominant factor in this increase is  
 530 the nature of how the power is calculated as the product of two measured  
 531 quantities (PMSM braking torque and rotational velocity), this leads to the  
 532 product of mean rotor velocity and torque variability becoming dominant in

533 power variability, explaining the dependence on rotor velocity. Similar values  
 534 for the variability in power and non-dimensional power coefficients were ob-  
 535 served for all test cases. Higher variability was expected for the IFREMER  
 536 test cases due to the presence of turbulence effects in these test cases. This  
 537 finding would suggest that the variability in power production measured via  
 538 the motor currents is dominated by measurement noise (common in motor  
 539 current measurements) and associated PMSM control functions rather than  
 540 the presence of low level turbulence. Lastly, the effect of torque control  
 541 rather than speed control seems to have made little difference to the mean  
 542 and standard deviations which are similar in magnitude for like facilities.

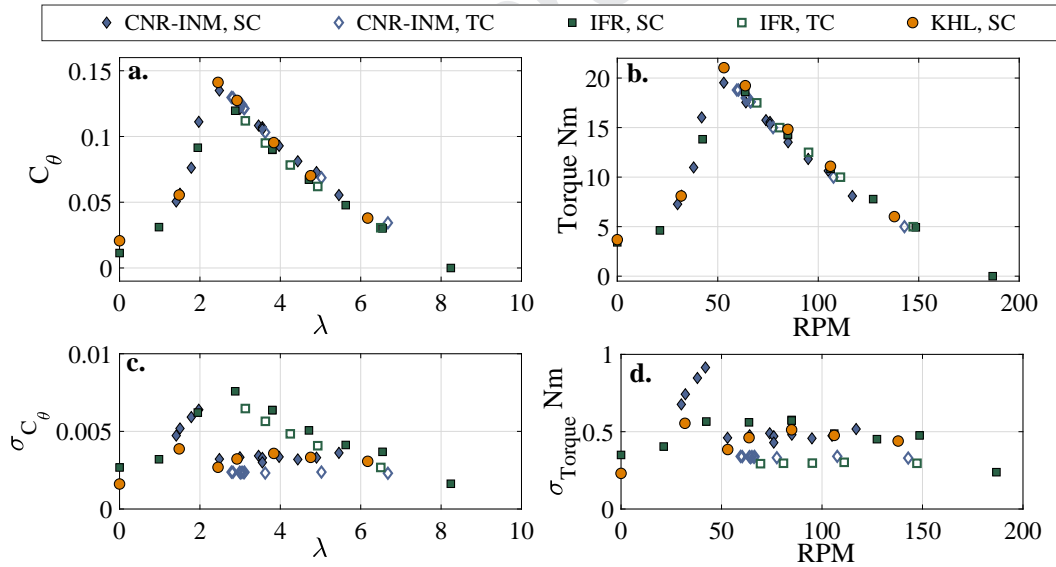


Figure 11: Blockage Corrected torque curves obtained whilst testing at CNR-INM, IFREMER and KHL. a) Shows Non-Dimensional torque coefficient against  $\lambda$ . b) Shows torque against RPM. c) Shows the standard deviation in non-dimensional torque coefficient against  $\lambda$ . d) Shows the standard deviation in torque against RPM.

543 Figure 11 shows that good agreement was found when comparing the

544 torque measurements from each facility. The blockage correction has had  
545 a significant effect on the  $C_\theta$  curves, which has resulted in very similar  $C_\theta$   
546 values for the CNR-INM and KHL test campaigns despite lower torsional  
547 values being recorded at CNR-INM, as shown by contrasting Figures 11a and  
548 11b. It can be seen in Figure 11a that the slight lower  $C_\theta$  value, presented  
549 in Table 7 for the IFREMER test case arises due to the operating points  
550 measured. It can be seen that the measurement points fall either side of  
551 peak torque, at  $\lambda \approx 2.5$  for the IFREMER test cases - although the shape of  
552 the curves observed for all facilities are similar.

553 The maximum standard deviation of torque and torque coefficients were  
554 of the order of 2 and 3 % of the mean values obtained, respectively. It  
555 can be seen that variability in torque produced by the rotor is of similar  
556 magnitude for each facility for  $\omega$ -values greater than  $\omega = 50$  RPM. Below this  
557 value all test cases show an increasing torque variability with increasing  $\omega$ ;  
558 the CNR-INM cases show the most severe torsional variability towards peak  
559 torque. In Figure 11d, it can be seen that the torsional variability was slightly  
560 higher for speed control cases than torque control cases, this is reflected in  
561  $C_\theta$  variability shown in Figure 11c. It can be seen that the variability in  
562  $C_\theta$  values measured at IFREMER follows closely the shape of the torque  
563 curves developed and shows generally higher variability, especially between  
564  $2 < \lambda < 6$ . This shows the dependence on the flow velocity variability  
565 when calculating  $\sigma_{C_\theta}$  via the standard variance propagation equations for  
566 independent variables. The similar levels of variability in torque for all speed  
567 control cases would suggest, again, that variability related to motor control  
568 is dominant over variability observed due to turbulence effects in the flume.

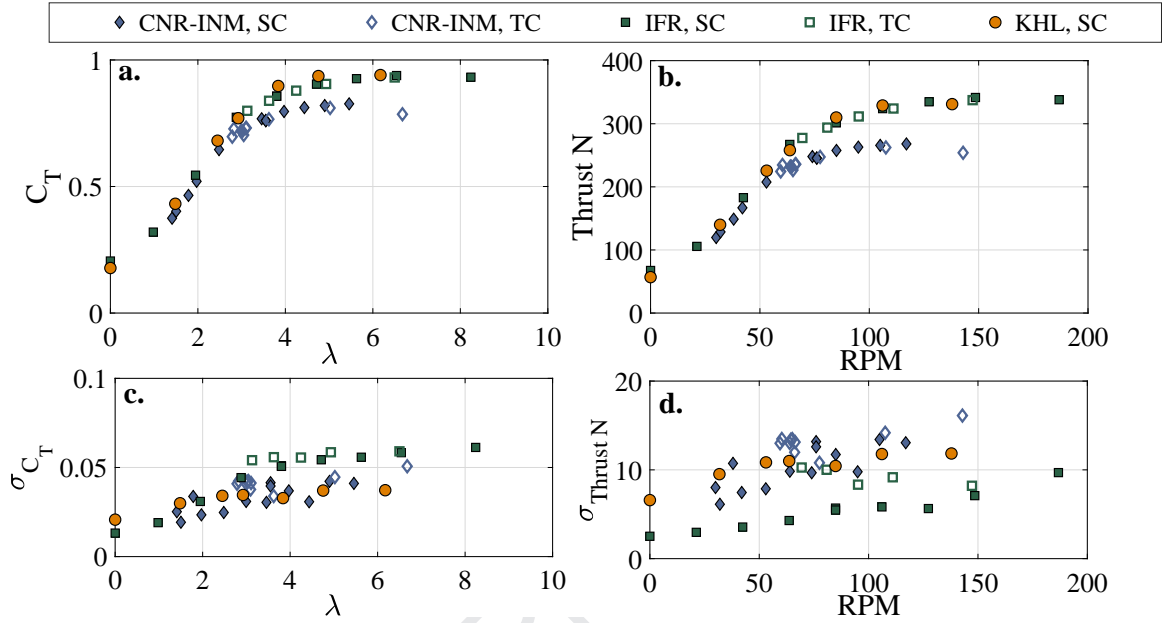


Figure 12: Blockage corrected thrust curves obtained whilst testing at both CNR-INM and IFREMER. a) Shows Non-Dimensional thrust coefficient against  $\lambda$ . b) Shows thrust against RPM. c) Shows the standard deviation in non-dimensional thrust coefficient against  $\lambda$ . d) Shows the standard deviation in thrust against RPM.

569 In Figure 12a and 12b the differing pitch settings between the CNR-INM  
 570 tests and the IFREMER and KHL cases are immediately apparent. Both the  
 571 raw thrust and blockage corrected non-dimensional thrust coefficient curves  
 572 show excellent agreement for the IFREMER and KHL cases. The  $C_T$  vs  $\lambda$   
 573 curve for CNR-INM are in agreement with the curves recorded from the other  
 574 facilities until approximately  $\lambda = 3.5$ , after this point the curves deviate in  
 575 shape with the CNR-INM curve becoming concave in shape as a drop-off in  
 576 thrust is observed at higher  $\lambda$ -values.

577 Again maximum standard deviation of thrust and thrust coefficients were  
 578 of the order of 3 and 3.5 % of the median values obtained, respectively. In-

579 teresting, the variability in thrust for the tow tank cases measured was found  
580 to be higher than those observed in the flume test cases. This unexpected  
581 result would suggest that the variability in the thrust loading observed at  
582 CNR-INM is driven by a combination of potential tow carriage velocity pre-  
583 cision, measurement noise and potential rotor imbalance. This is supported  
584 in that relatively similar standard deviations in the thrust coefficient were  
585 observed at the IFREMER test facility for similar levels of turbulence and  
586 reported in [27]. Regarding the CNR-INM data, intermittent noise spikes  
587 were observed in the thrust data. To combat this additional shielding was  
588 added between testing at CNR-INM and IFREMER. Regarding the root  
589 causes of the unexpected variability observed at KHL, further analysis will  
590 be required to fully understand the unexpected result. Lastly, both thrust  
591 and non-dimensional thrust coefficient are affected by the control strategy  
592 adopted, exhibiting slightly higher thrust variations under the torque control  
593 cases which has been observed previously [19][26].

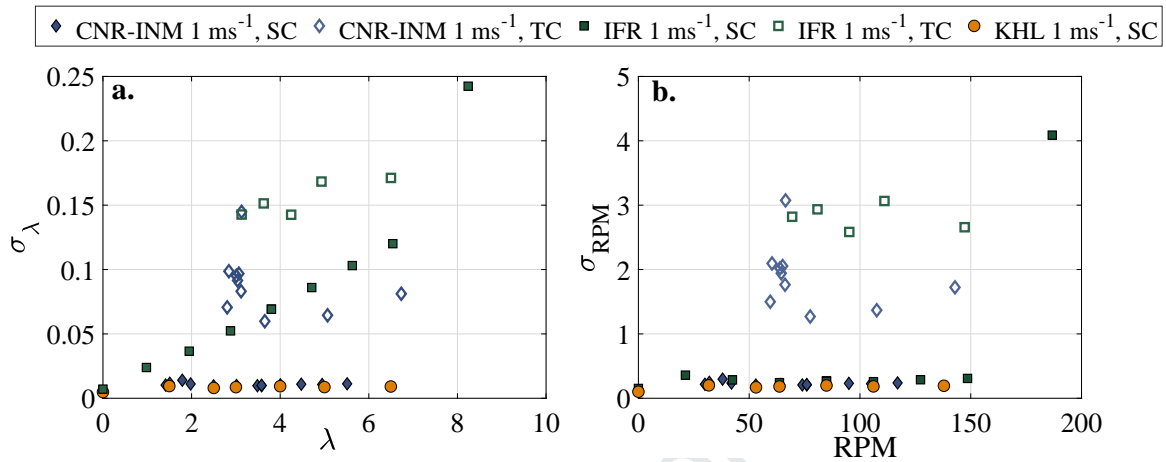


Figure 13: Figure showing the standard deviation of  $\lambda$  values against  $\lambda$  (left) and the standard deviation of RPM against RPM (right).

594 Figure 13 shows the standard deviation of the  $\lambda$ -values and RPMs ob-  
 595 served at each of the facilities. It is immediately clear that the control  
 596 strategy has major effect on the variability of the turbine operating point  
 597 during testing - this is in agreement with the higher thrust and torque fluc-  
 598 tuations observed for the torque control case. A discrepancy between the  
 599 non-dimensional kinematic quantity  $\lambda$  and the RPM standard deviations is  
 600 exhibited for the IFREMER test case. The increasing trend in standard de-  
 601 viation observed in Figure 13a would seem to be generated in the variance  
 602 propagation calculations made. This would suggest that covariance between  
 603 quantities is significant and should be used in such calculations.

#### 604 5.4.2. Three Turbine Characterisation at KHL

605 Figures 14 to 18 show the data sets for the three turbines tested at the  
 606 KHL providing the characteristic curves of  $C_P$ ,  $C_\theta$ ,  $C_T$ ,  $M_x$  and  $M_z$  for the  
 607 0.8, 1.0 and 1.2  $m s^{-1}$  carriage velocity cases. The plots are based on the rotor

608 and blade transducer data recorded; in addition  $C_P$  and  $C_\theta$  derived utilising  
609 PMSM winding current measurements are also presented, which clearly show  
610 the drive train losses. Spline fits to the data have been included for clarity  
611 and to highlight the underlying nature of the characteristic curves measured.  
612 Table 8 shows the peak quantities observed in the rotor data. Table 8 also  
613 shows the maximum standard deviation observed for each non-dimensional  
614 quantity at the peak operating point as well as the range of non-dimensional  
615 values observed between differing turbines as a percentage of the peak value.  
616 The author's note that due to water ingress into the nose cone of T1 during  
617 the experiments at KHL, no blade data was captured as such these plots are  
618 omitted from Figures 17 and 18. Furthermore, due to the timing restraints  
619 on the testing the water ingress meant it was only possible to test T1 at the  
620 0.8 and 1.0  $ms^{-1}$ . Since this time the cause of the leak has been detected  
621 and rectified.

Table 8: Table providing an overview of peak non-dimensional quantities observed, with standard deviations for a given turbine presented as well as the range of non-dimensional values recorded across the three turbines.

<b>Qty</b>	<b>Turbine 1</b>	<b>Turbine 2</b>	<b>Turbine 3</b>
Max $C_P$	0.47	0.48	0.48
U @ Max $C_P$	$1.0 \text{ m s}^{-1}$	$0.8 \text{ m s}^{-1}$	$1.0 \text{ m s}^{-1}$
$\lambda$ @ Max $C_P$	4	4	4
Max $\sigma_{C_P}$ @ $\lambda = 4$	0.013	0.015	0.013
Range $C_P$ @ $\lambda = 4$ % of Max $C_P$	6.7 %		
Max $C_\theta$	0.16	0.17	0.16
U @ Max $C_\theta$	$1.0 \text{ m s}^{-1}$	$1.0 \text{ m s}^{-1}$	$1.2 \text{ m s}^{-1}$
$\lambda$ @ Max $C_\theta$	2.5	2.5	2.5
Max $\sigma_{C_\theta}$ @ $\lambda = 2.5$	0.003	0.003	0.003
Range $C_\theta$ @ $\lambda = 2.5$ % of Max $C_\theta$	4.2 %		
Max $C_T$	1.05	1.09	1.09
U @ Max $C_T$	$0.8 \text{ m s}^{-1}$	$0.8 \text{ m s}^{-1}$	$0.8 \text{ m s}^{-1}$
$\lambda$ @ Max $C_T$	5	6.5	6.5
Max $\sigma_{C_T}$ @ $\lambda = 6.5$	0.05	0.02	0.02
Range $C_\theta$ @ $\lambda = 2.5$ % of Max $C_T$	6.8 %		

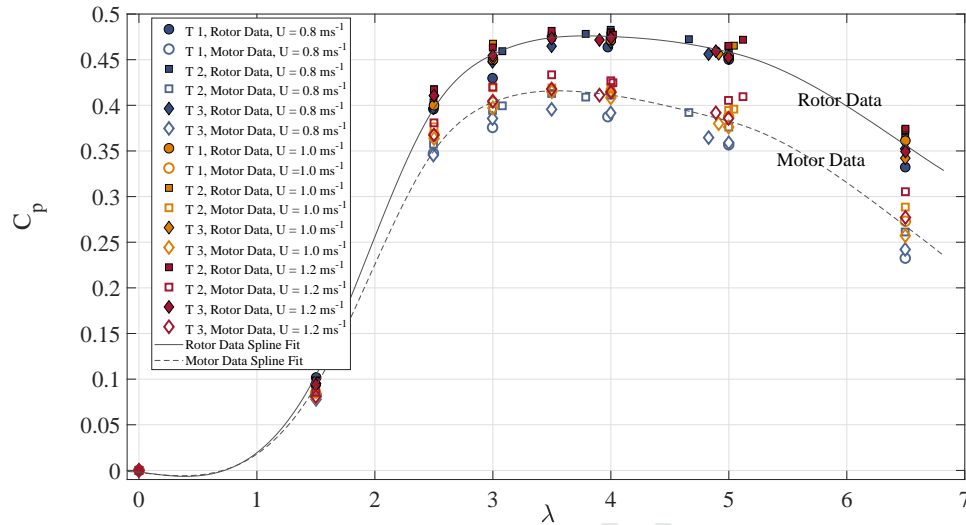


Figure 14: Characteristic power curves obtained whilst testing at KHL for each of the three turbines, the figures show both the power curves obtained considering rotor transducer measurements and motor power measurements.

622 In all cases the non-dimensional characteristics display a very good level  
 623 of repeatability, not only for each turbine at the separate velocities, but  
 624 also when comparing each of the differing turbines manufactured. With  
 625 reference to Figure 14, the largest spread of  $C_p$  values recorded was found  
 626 at the highest  $\lambda$ -value tested, namely  $\lambda = 6.5$ . This spread was found to be  
 627 larger in the  $C_p$  values derived from the motor data rather than the rotor  
 628 transducer. This would suggest, as asserted above, that motor control actions  
 629 (including winding current measurement noise) generally yield more variable  
 630 power measurements than the rotor transducer for low turbulence operation.  
 631 Drive shaft losses, taken as the difference between the motor data derived  
 632  $C_p$  and the rotor transducer derived  $C_p$ , were found to increase with  $\lambda$  and  
 633 ranged from 11% in the peak power region up to 21% at free-wheeling. The

634 losses for all three turbines were consistent, however it was found that slightly  
 635 higher losses were found for the  $0.8 \text{ ms}^{-1}$  carriage speed case. Due to these  
 636 losses, the nature of the  $C_P$  curves developed vary between those measured  
 637 via the motor data and the rotor transducer. Peak  $C_P$  derived via the motor  
 638 data was found to arise at  $3 < \lambda < 4$ . Whereas the peak power in the rotor  
 639 transducer data arose at  $\lambda = 4$ . This distortion of the power curves can be  
 640 expected as the losses found were not consistent across operating points with  
 641 aforementioned dependence on rotational velocity.

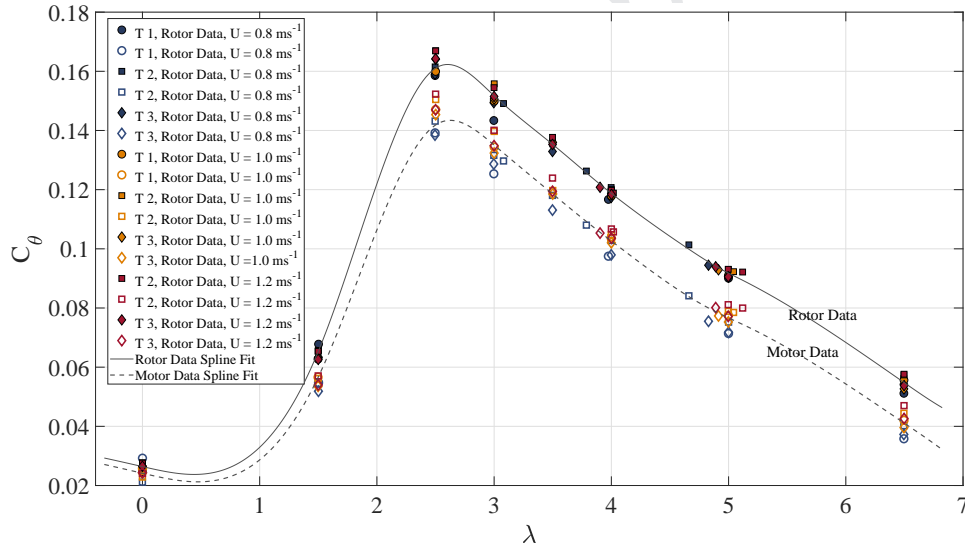


Figure 15: Characteristic torque curves obtained whilst testing at KHL for each of the three turbines, the figures show both the power curves obtained considering rotor transducer measurements and motor power measurements.

642 The non-dimensional torque coefficients observed for the KHL test cases  
 643 again show good agreement over both differing fluid velocities and for dif-  
 644 fering turbines, Figure 15. A peak rotor based  $C_\theta$  value of 0.16 was found  
 645 at  $\lambda = 2.5$ , which coincides with the findings from the other test facilities

646 discussed in Section 5.4.1. Again, the  $C_\theta$  values calculated via motor current  
 647 measurements a more widely spread than the rotor transducer based values.  
 648 Likewise, the motor data based values for the  $0.8 \text{ ms}^{-1}$  case were generally  
 649 found to be slightly lower than the other fluid velocity cases. Increased data  
 650 spread can be observed in the peak torque region as well as the at high  
 651  $\lambda$ -values.

652 Figure 16 shows very good agreement for the non-dimensional thrust co-  
 653 efficients observed across all test cases. Minimal scatter is observed until a  
 654  $\lambda$  value of 6.5, where a maximum  $C_T$  of 1.09 was observed. Given the afore-  
 655 mentioned sensitivity of the thrust loading experience to blade pitch angle  
 656 setting, this would suggest high repeatability in blade pitch angle setting.

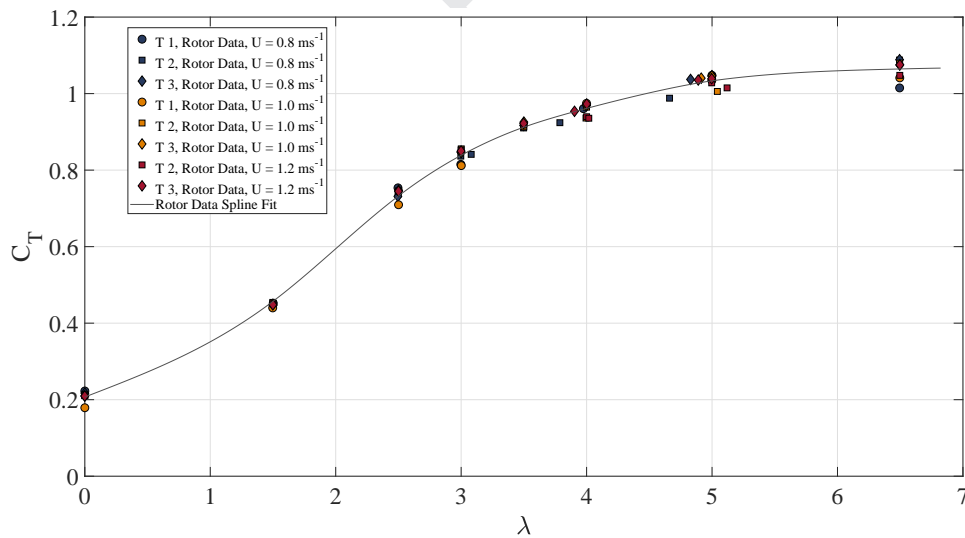


Figure 16: Characteristic thrust curves obtained whilst testing at KHL for each of the three turbines

657 The individual blade axial moments shown in Figure 17, show an excellent  
 658 grouping with each turbine comparable to the other turbines. Figure 18

659 shows the  $M_z$  moment operating in the rotational direction. There is clearly  
660 a wide spread of the data sets both between each blade for the same turbine  
661 and also for the additional and identical turbines. What can be extracted  
662 from the data sets is that they follow the same trend, as shown in Figure 15,  
663 for the torque loading over the range of  $\lambda$  values, peaking at  $\lambda \approx 2.5$  in all  
664 cases.

665 The non-dimensional parameters and blade root bending moment curves  
666 have shown that the design and manufacture of the individual turbines is of  
667 a quality that allows interchangeability and repeatability. Testing of mul-  
668 tiple turbines can be directly compared to the data sets for the individual  
669 turbines providing high levels of confidence and reliability. The introduction  
670 of turbulence, wakes, wave-current interaction, current-structural interaction  
671 or in fact any combination can be directly compared to these data sets to  
672 determine their influence of the dynamic loading of the turbines.

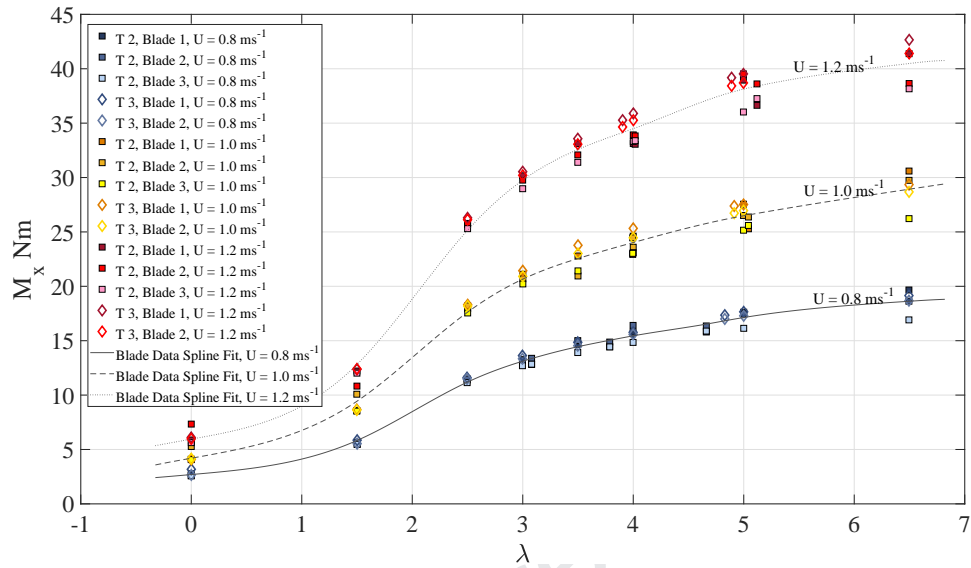


Figure 17: Characteristic blade root bending moments, flapwise or  $M_x$  moments, obtained whilst testing at KHL for each of the three turbines

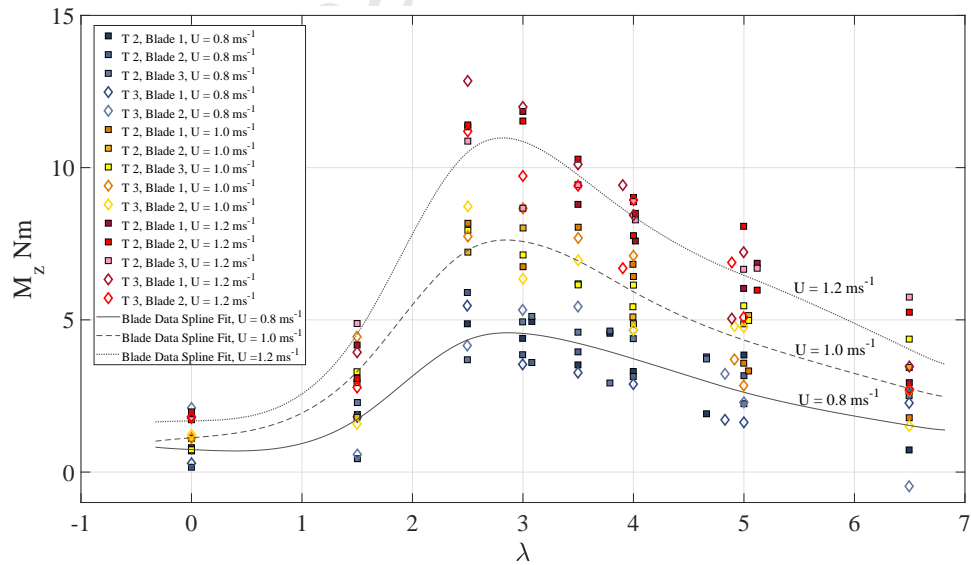


Figure 18: Characteristic blade root bending moments, edgewise or  $M_z$  moments, obtained whilst testing at KHL for each of the three turbines

673 *5.5. Discussion*

674 The results section presents the data relating to a variety of test cam-  
675 paigns for a single turbine, namely T1, followed by a comparison of the  
676 non-dimensional parameters of the three turbines manufactured to the spec-  
677 ifications detailed throughout the paper.

678 The comparison of the findings from the differing test campaigns shows  
679 that relatively repeatable results were generated. However, some significant  
680 differences were highlighted between the findings. The authors note that this  
681 was not entirely unexpected as these tests were performed at differing stages  
682 of development and design integration for the prototype turbine, turbine  
683 T1. These results, in terms of power and torque, were generated by utilising  
684 PMSM winding current measurements. The relatively large spread in the  
685 data and the deviation of the power curve recorded at IFREMER relative to  
686 the tow tank cases, suggests that detailed understanding and characterisation  
687 of motor control operations and drive shaft losses are required to generate  
688 concrete findings when using motor current data to measure rotor power  
689 and torque. Furthermore, it was considered that changes in the turbine  
690 set-up during development are likely to have changed the drive train losses  
691 characterisation - this may have impacted on the blockage correction method  
692 utilised by changing the power to thrust relationship of the turbine.

693 Another aspect of deviation between the test cases was the differing thrust  
694 characteristics observed during the testing undertaken at CNR-INM relative  
695 to the latter test cases. This was largely attributed to the differing pitch  
696 angle settings tested at CNR-INM relative to the test campaigns undertaken  
697 at IFREMER and KHL. The differing pitch angle settings were tested to

698 confirm the relative insensitivity to pitch angle variations between  $6^\circ$  and  $9^\circ$   
699 of the power produced. The inverse finding for rotor thrust was also found,  
700 as expected based on the BEMT and CFD modelling. Whilst the finding  
701 of the modelling stages seem to have been confirmed, the authors believe  
702 a structured test campaign is required to fully quantify the effects of pitch  
703 angle on power and thrust production.

704 The variability observed between facilities was of a similar magnitude  
705 which was unexpected due to the presence of approximately 2 % turbulence  
706 intensity experienced at IFREMER. This highlights the requirement for high  
707 levels of electrical shielding, a high degree of accuracy in rotor and drive  
708 train set-up and the requirement to measure rotor quantities directly. This  
709 finding is non-trivial in the quantification of dynamic loading and suggested  
710 that before undertaking more ambitious test campaigns including unsteady  
711 effects, such as testing under wave conditions and high levels of turbulence,  
712 an initial set of steady-state tests at the given facility should be undertaken  
713 as a benchmark.

714 Lastly, the mean non-dimensional quantities observed at the KHL facility  
715 for all three of the manufactured turbines showed good agreement. As such,  
716 there is a high level certainty in the turbine characterisations performed.  
717 Relatively large scatter was found for the blade root bending moment mea-  
718 surements taken. These results suggest that improved amplification and  
719 filtering of the blade root bending moment measurements maybe required,  
720 although it cannot be concluded at this stage that the differing quantities  
721 observed are spurious findings.

722 *5.6. Conclusions and Further Work*

723 The paper presents the specification of a 1/20th scale HATT design, de-  
724 tailing blade design activities as well as measurement and turbine control  
725 processes. The paper then outlines testing of the three lab scale HATTs.

726 The updated blade design yielded higher turbine performance with a rel-  
727 atively minor increase in thrust loading. A maximum  $C_P$  of 0.47 at  $\lambda = 4$   
728 was observed with a maximum  $C_T$  of 1.09 found for  $\lambda$  values above 6.5.  
729 Free-wheeling occurred at  $\lambda = 8$ , with peak torque at  $\lambda = 2.5$ .

730 The operation and design of the turbine and its instrumentation was  
731 demonstrated across the various test campaigns. Under speed control the  
732 standard deviation of the rotational velocity of the turbine was, in most cases,  
733 below 0.3 RPM, other than at free-wheeling. Under torque control torsional  
734 variations of 0.4 Nm were observed. The quantities represent variability of  
735 less than 2.5 % relative to median values and demonstrated a high degree of  
736 stability in the turbine control systems across all operating ranges.

737 Good agreement between the tests undertaken at differing facilities was  
738 found given the development and maintenance of the turbine between test  
739 campaigns. It was found that using motor current measurements to estimate  
740 turbine rotor torque and power can lead to uncertainty in results if a high  
741 degree of characterisation of motor control variability and drive shaft losses  
742 are not undertaken. Furthermore, it was found that it is not clear the effect of  
743 drive shaft losses on the blockage correction approach which will change the  
744 power to thrust characteristics for the turbine. A high degree of repeatability  
745 of the rotor quantities across all three turbines was confirmed via the test  
746 campaign undertaken at the KHL.

747 Further work is being undertaken to generate an in-depth characterisation  
748 of the three turbines tested at the KHL. This work will seek to understand in  
749 more detail the dynamic aspects associated with the turbine operation and  
750 the discrepancies between the turbines in this regard. The blade root bending  
751 moment instrumentation will be further developed with greater amplification  
752 and filtering to improve measurement consistency. Lastly, the three turbines  
753 have been tested in a variety of dynamic conditions, the findings relating  
754 to these campaigns will be presented in future. Furthermore, the turbines  
755 detailed have been utilised for array characterisation at FloWave, Edinburgh  
756 and will be used for detailed flow characterisation of two interacting turbines,  
757 with this test campaign being undertaken at IFREMER.

## 758 **Acknowledgements**

759 Funding: This work was supported by the Engineering and Physical Sci-  
760 ences Research Council [DyLoTTA –EP/N020782/1]; Horizon2020 [MARINET2-  
761 731084]; Engineering and Physical Sciences Research Council [Cardiff Univer-  
762 sity Impact Acceleration Account-EP/R51150X/1].

763 [1] Department of Energy & Climate Change, DECC Electricity Gen-  
764 eration Costs 2013 - GOV.UK, Tech. rep., Department of Energy &  
765 Climate Change, London (2013).

766 URL <https://www.gov.uk/government/publications/decc-electricity-generation-co>

767 [2] X.-P. Zhang, P. Zeng, Marine Energy Technology [Scanning  
768 the Issue], Proceedings of the IEEE 101 (4) (2013) 862–865.  
769 doi:10.1109/JPROC.2013.2244735.

770 [3] European Parliament, Directive (EU) 2018/2001 of the European  
771 Parliament and of the Council of 11 December 2018 on the promotion  
772 of the use of energy from renewable sources, Tech. rep., European  
773 Parliament and Council of 11 December 2018, London (2018).

774 URL [https://eur-lex.europa.eu/legal-content/EN/ALL/?uri=uriserv:OJ.L\\_.2018.32](https://eur-lex.europa.eu/legal-content/EN/ALL/?uri=uriserv:OJ.L_.2018.32)

775 [4] C. Johnstone, D. Pratt, J. Clarke, A. Grant, A techno-economic anal-  
776 ysis of tidal energy technology, *Renewable Energy* 49 (2013) 101–106.  
777 doi:10.1016/J.RENENE.2012.01.054.

778 [5] IEC, IEC 61400 - Wind turbines, Tech. rep., IEC (2015).

779 URL <https://webstore.iec.ch/publication/22259>

780 [6] A. Bahaj, A. Molland, J. Chaplin, W. Batten, Power and thrust mea-  
781 surements of marine current turbines under various hydrodynamic flow  
782 conditions in a cavitation tunnel and a towing tank, *Renewable Energy*  
783 32 (3) (2007) 407–426. doi:10.1016/J.RENENE.2006.01.012.

784 [7] J. A. Clarke, G. Connor, A. D. Grant, C. M. Johnstone, Design and  
785 testing of a contra-rotating tidal current turbine, *Proceedings of the In-*  
786 *stitution of Mechanical Engineers, Part A: Journal of Power and Energy*  
787 221 (2) (2007) 171–179. doi:10.1243/09576509JPE296.

788 [8] T. Stallard, R. Collings, T. Feng, J. Whelan, Interactions between tidal  
789 turbine wakes: experimental study of a group of three-bladed rotors,  
790 *Philosophical Transactions of the Royal Society A: Mathematical, Phys-*  
791 *ical and Engineering Sciences* 371 (1985) (2013) 20120159–20120159.  
792 doi:10.1098/rsta.2012.0159.

- 793 [9] P. Mycek, B. Gaurier, G. Germain, G. Pinon, E. Rivoalen, Numerical  
794 and experimental study of the interaction between two marine current  
795 turbines, *International Journal of Marine Energy* 1 (2013) 70–83.  
796 doi:10.1016/j.ijome.2013.05.007.
- 797 [10] P. Mycek, B. Gaurier, G. Germain, G. Pinon, E. Rivoalen, Experimental  
798 study of the turbulence intensity effects on marine current turbines be-  
799 haviour. Part II: Two interacting turbines, *Renewable Energy* 68 (2014)  
800 876–892. doi:10.1016/J.RENENE.2013.12.048.
- 801 [11] P. Mycek, B. Gaurier, G. Germain, G. Pinon, E. Rivoalen, Experimental  
802 study of the turbulence intensity effects on marine current turbines  
803 behaviour. Part I: One single turbine, *Renewable Energy* 66 (2014) 729–  
804 746. doi:10.1016/J.RENENE.2013.12.036.
- 805 [12] G. S. Payne, T. Stallard, R. Martinez, Design and manufacture of a bed  
806 supported tidal turbine model for blade and shaft load measurement  
807 in turbulent flow and waves, *Renewable Energy* 107 (2017) 312–326.  
808 doi:10.1016/J.RENENE.2017.01.068.
- 809 [13] A. Mason-Jones, Performance assessment of a Horizontal Axis Tidal  
810 Turbine in a high velocity shear environment., Ph.D. thesis, Cardiff  
811 University (2010).
- 812 [14] M. J. Allmark, Condition monitoring and fault diagnosis of tidal stream  
813 turbines subjected to rotor imbalance faults, Ph.D. thesis, Cardiff Uni-  
814 versity (2016).

- 815 [15] C. Frost, C. E. Morris, A. Mason-Jones, D. M. O'Doherty,  
816 T. O'Doherty, The effect of tidal flow directionality on tidal tur-  
817 bine performance characteristics, *Renewable Energy* 78 (2015) 609–620.  
818 doi:10.1016/j.renene.2015.01.053.
- 819 [16] C. Morris, Influence of solidity on the performance, swirl characteristics,  
820 wake recovery and blade deflection of a horizontal axis tidal turbine,  
821 Ph.D. thesis, Cardiff University (2014).
- 822 [17] M. Allmark, R. Grosvenor, P. Prickett, An approach to the characteri-  
823 sation of the performance of a tidal stream turbine, *Renewable Energy*  
824 111 (2017) 849–860. doi:10.1016/j.renene.2017.05.010.  
825 URL <http://linkinghub.elsevier.com/retrieve/pii/S0960148117303956>
- 826 [18] S. Ordonez-Sanchez, R. Ellis, K. Porter, M. Allmark, T. O'Doherty,  
827 A. Mason-Jones, C. Johnstone, Numerical models to pre-  
828 dict the performance of tidal stream turbines working under  
829 off-design conditions, *Ocean Engineering* 181 (2019) 198–211.  
830 doi:10.1016/J.OCEANENG.2019.04.027.  
831 URL <https://www.sciencedirect.com/science/article/pii/S0029801818312848>
- 832 [19] S. Ordonez Sanchez, K. Porter, C. Frost, M. Allmark, C. Johnstone,  
833 T. O'Doherty, Effects of extreme wave-current interactions on the per-  
834 formance of tidal stream turbines, in: 3rd Asian Wave and Tidal Energy  
835 Conferenece, Singapore, 2016.
- 836 [20] A. Mason-Jones, D. O'Doherty, C. Morris, T. O'Doherty, C. Byrne,  
837 P. Prickett, R. Grosvenor, I. Owen, S. Tedds, R. Poole, Non-dimensional

- 838 scaling of tidal stream turbines, *Energy* 44 (1) (2012) 820–829.  
839 doi:10.1016/J.ENERGY.2012.05.010.
- 840 [21] D. Egarr, T. O’doherly, S. Morris, R. Ayre, Feasibility study using com-  
841 putational fluid dynamics for the use of a turbine for extracting energy  
842 from the tide, in: 15th Australasian Fluid Mechanics Conference, 2004.  
843 doi:10.13140/2.1.4852.3041.
- 844 [22] T. Nevalainen, C. Johnstone, A. Grant, A sensitivity analysis on tidal  
845 stream turbine loads caused by operational, geometric design and inflow  
846 parameters, *International Journal of Marine Energy* 16 (2016) 51–64.  
847 doi:10.1016/J.IJOME.2016.05.005.
- 848 [23] R. Ellis, M. Allmark, T. O’Doherty, A. Mason-Jones, S. Ordonez-  
849 Sanchez, K. Johannesen, C. Johnstone, Design process for a scale hor-  
850 izontal axis tidal turbine blade, in: 4th Asian Wave and Tidal Energy  
851 Conference, Taipei, 2018.
- 852 [24] F. R. Menter, A comparison of some recent eddy-viscosity turbulence  
853 models, *Journal of Fluids Engineering, Transactions of the ASME*  
854 118 (3) (1996) 514–519. doi:10.1115/1.2817788.
- 855 [25] S. A. El-Shahat, G. Li, F. Lai, L. Fu, Investigation of parame-  
856 ters affecting horizontal axis tidal current turbines modeling by blade  
857 element momentum theory, *Ocean Engineering* 202 (2020) 107176.  
858 doi:10.1016/j.oceaneng.2020.107176.
- 859 [26] S. Ordonez-Sanchez, M. Allmark, K. Porter, R. Ellis, C. Lloyd, I. Santic,  
860 T. O’Doherty, C. Johnstone, Analysis of a Horizontal-Axis Tidal Turbine

- 861 Performance in the Presence of Regular and Irregular Waves Using Two  
 862 Control Strategies, *Energies* 12 (3) (2019) 367. doi:10.3390/en12030367.  
 863 URL <http://www.mdpi.com/1996-1073/12/3/367>
- 864 [27] B. Gaurier, G. Germain, J. Facq, C. Johnstone, A. Grant, A. Day,  
 865 E. Nixon, F. Di Felice, M. Costanzo, Tidal energy “Round Robin”  
 866 tests comparisons between towing tank and circulating tank re-  
 867 sults, *International Journal of Marine Energy* 12 (2015) 87–109.  
 868 doi:10.1016/J.IJOME.2015.05.005.  
 869 URL <https://www.sciencedirect.com/science/article/pii/S2214166915000223>
- 870 [28] BS 8422:2003 - Force measurement. Strain gauge load cell systems.  
 871 Calibration method, Tech. rep., BSI (2003). doi:0 580 42746 3.  
 872 URL <https://shop.bsigroup.com/ProductDetail/?pid=000000000030067617>

### 873 **Appendix A. Consideration of Reynolds Effects**

874 To confirm the comparisons made in Sections 5.4.1 and 5.4.2 were not sub-  
 875 ject to Reynolds effects, a comparison of non-dimensional quantities for tests  
 876 undertaken at differing flow speeds and associated chord based Reynold’s  
 877 numbers undertaken at IFREMER were considered. Figure A.19 shows  
 878 the non-dimensional power coefficient distribution for differing chord based  
 879 Reynolds numbers. Here the chord based Reynolds number is defined as:

$$RE_{0.7Chord} = \frac{\rho \cdot C_{0.7} \cdot U}{\mu} \quad (\text{A.1})$$

880 where,  $\rho$  is the fluid density in  $kgm^{-3}$ ,  $C_{0.7}$  is the chord length at 70 % of  
 881 the radius in  $m$ ,  $U$  is the mean fluid velocity in  $ms^{-1}$  and  $\mu$  is the dynamic

882 viscosity in  $Pa \cdot s$ . Figure A.19 shows that Reynolds effects become negligible,  
 883 with a variation of 1 %, for Reynold's numbers above  $RE_{0.7Chord} = 6.48E+4$ .

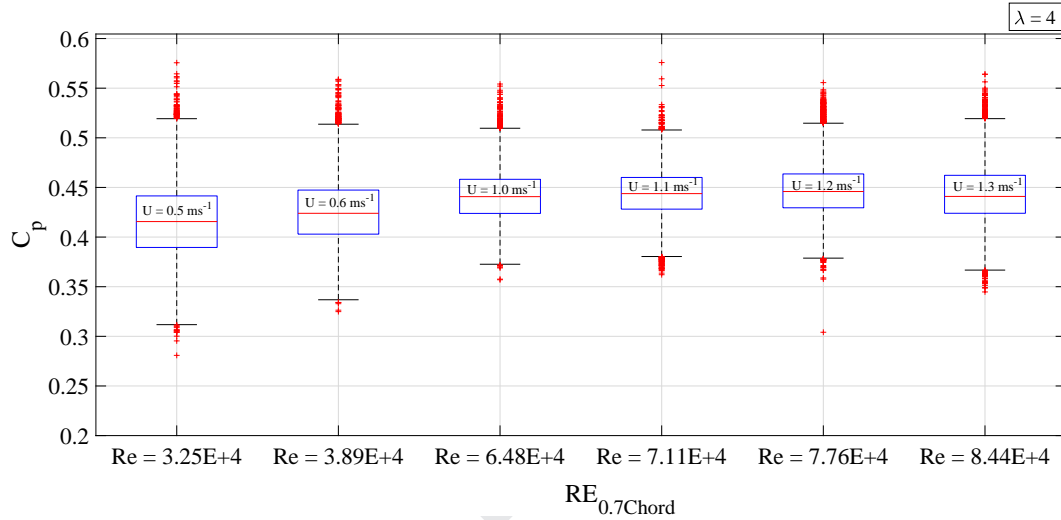


Figure A.19: Comparison of  $C_P$  values observed for tests under taken at differing fluid velocities. The  $C_P$  values are plotted against chord length based Reynold's Number for a fixed  $\lambda$ -value of  $\lambda = 4$ .

## 884 Appendix B. Instrumentation Calibration

### 885 Appendix B.0.1. Rotor Thrust and Torque Transducer Calibrations

886 The rotor thrust and torque transducers were calibrated by applied mea-  
 887 surements. Calibration certificates were provided with the transducers de-  
 888 tailing the calibrations undertaken and reporting on non-linearity, hysteresis  
 889 and cross-axis sensitivity.

Table B.9: Summary of calibration results for the 3 torque thrust transducers as undertaken by Applied Measurements Ltd.

Qty	Turbine 1	Turbine 2	Turbine 3
Serial No.	54283	54284	157961
Thrust Gradient, A/N	5.308E-3	5.349E-3	5.333E-3
Thrust non-linearity	$\pm 0.043\%$ FS	$\pm 0.056\%$ FS	$\pm 0.043\%$ FS
Thrust hysteresis	$< 0.074\%$ FS	$< 0.098\%$ FS	$< 0.074\%$ FS
Thrust cross-sensitivity	$< 0.23\%$ FS	$< 0.45\%$ FS	$< 0.23\%$ FS
Torque Gradient, A/Nm	8.00E-2	8.01E-2	8.00E-2
Torque non-linearity	$\pm 0.031\%$ FS	$\pm 0.031\%$ FS	$\pm 0.031\%$ FS
Torque hysteresis	$< 0.075\%$ FS	$< 0.062\%$ FS	$< 0.075\%$ FS
Torque cross-sensitivity	$< 0.35\%$ FS	$< 0.18\%$ FS	$< 0.35\%$ FS

890 *Appendix B.0.2. Flap-Wise Blade Root Bending Moment Calibrations*

891 The three flap-wise blade root bending moment transducers for each tur-  
892 bine were calibrated according to the BSI - standard [28]. Increasing moments  
893 were applied to the transducers and the current output from the amplifiers  
894 were recorded in Amps. The weights used to create the moments had an  
895 uncertainty of 0.001g with the distance over which the load was applied had  
896 an uncertainty of 0.1 mm. Figures B.20 and B.21 show the calibration and  
897 residuals associated with the linear fit for hub 1, blade 2. Tables B.10 to B.12  
898 show the gradients and uncertainties for each of the calibrated transducers.

Table B.10: Summary of calibration results for flap-wise blade root bending moment transducers, Turbine 1.

<b>Qty</b>	<b>Blade 1</b>	<b>Blade 2</b>	<b>Blade 3</b>
Gradient A/Nm	1.59E-4	1.62E-4	1.57E-4
Fit Uncertainty (SEE), Nm	0.62	0.45	0.44
Bias Uncertainty, Nm	0.12	0.12	0.12
Total Uncertainty, Nm	0.63	0.47	0.46

Table B.11: Summary of calibration results for flap-wise blade root bending moment transducers, Turbine 2.

<b>Qty</b>	<b>Blade 1</b>	<b>Blade 2</b>	<b>Blade 3</b>
Gradient A/Nm	1.60E-4	1.63E-4	1.62E-4
Fit Uncertainty (SEE), Nm	0.43	0.41	0.90
Bias Uncertainty, Nm	0.12	0.12	0.12
Total Uncertainty, Nm	0.45	0.43	0.90

Table B.12: Summary of calibration results for flap-wise blade root bending moment transducers, Turbine 3.

<b>Qty</b>	<b>Blade 1</b>	<b>Blade 2</b>	<b>Blade 3</b>
Gradient A/Nm	1.60E-4	1.62E-4	NA
Fit Uncertainty (SEE), Nm	0.41	0.42	NA
Bias Uncertainty, Nm	0.12	0.12	NA
Total Uncertainty, Nm	0.43	0.44	NA

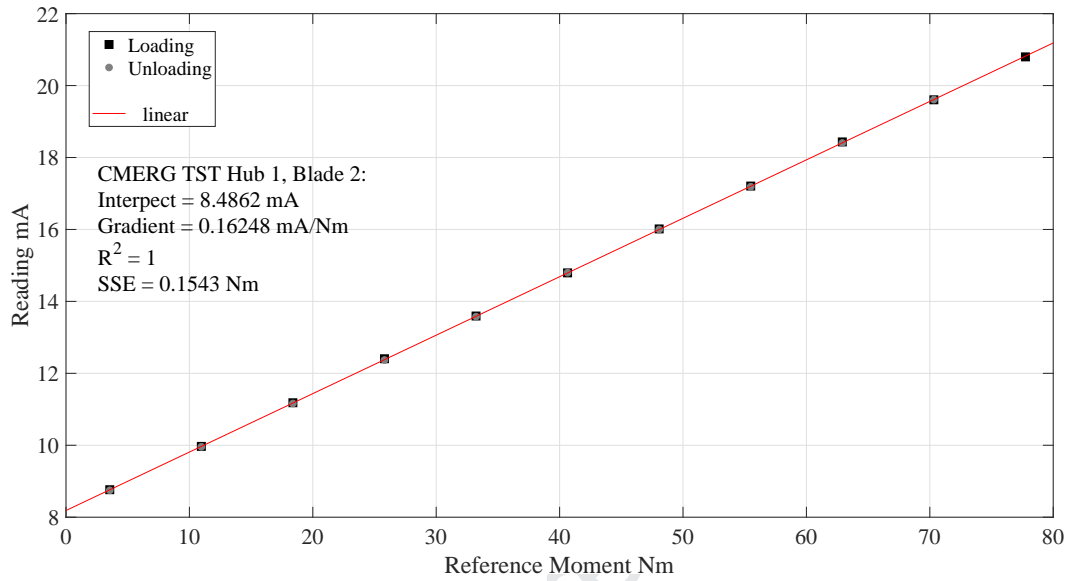


Figure B.20: The calibration results for the flapwise blade root bending moment transducer for blade 2, hub 1.

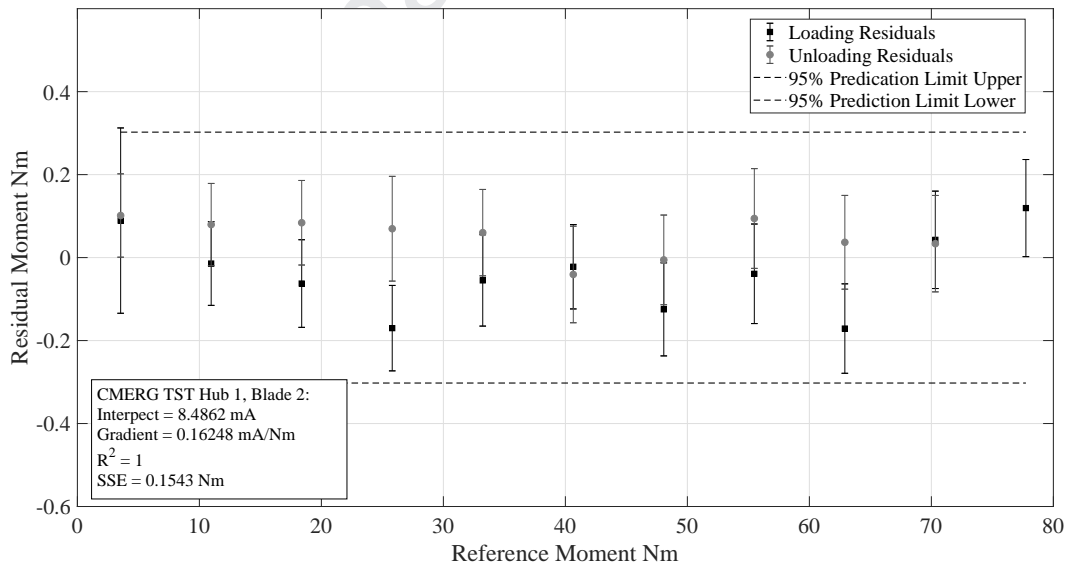


Figure B.21: Fitted residuals for calibration results for the flapwise blade root bending moment transducer for blade 2, hub 1.

899 *Appendix B.0.3. Edge-Wise Blade Root Bending Moment Calibrations*

900 The edge-wise blade root bending moment calibrations were undertaken  
901 in-situ comparing the outputs from the blade root bending moment trans-  
902 ducers with the outputs from the calibrated rotor torque transducer. In this  
903 way the relationship in Equation B.1 was assumed to hold for mean quanti-  
904 ties. Furthermore, it was assumed that the mean edge-wise bending moment  
905 from each blade was equal for a given test. This method gave relatively good  
906 results, however large uncertainties were found and can be seen in the spread  
907 of data in Figure 18. Improved calibrations for this measurement are being  
908 undertaken for subsequent test campaigns.

$$\bar{\tau}_{rotor} = \sum_{i=1}^3 M_{zi} \quad (\text{B.1})$$

The development, design and characterisation of a scale model Horizontal Axis Tidal Turbine for Dynamic Load Quantification

HIGHLIGHTS:

- Outlines the development of three 1/20<sup>th</sup> scale horizontal axis tidal turbines.
- Presents the blade development undertaken to create an optimum turbine rotor.
- Details of the drivetrain, instruments and control systems design are given.
- Tests at differing facilities and the same facility for similar devices presented.
- The paper discusses aspects of good practice for flume/tow-tank testing.

**Declaration of interests**

The authors declare that they have no known competing financial interests or personal relationships that could have appeared to influence the work reported in this paper.

The authors declare the following financial interests/personal relationships which may be considered as potential competing interests: